**Flood extent mapping during Hurricane Florence with repeat-pass L-band UAVSAR images**

Chao Wang[1], Tamlin M. Pavelsky[1], Fangfang Yao[2], Xiao Yang[1], Shuai Zhang[3], Bruce Chapman[4], Conghe Song[5], Antonia Sebastian[1], Brian Frizzelle[6], Elizabeth Frankenberg[7], Nicholas Clinton[8]

[1]Department of Geological Sciences, University of North Carolina, Chapel Hill, NC, USA

[2]CIRES University of Colorado Boulder, Boulder, CO, USA

[3]College of Marine Science, University of South Florida, St. Petersburg, FL, USA

[4]Jet Propulsion Laboratory, California Institute of Technology, Pasadena, CA, USA

[5]Department of Geography, University of North Carolina, Chapel Hill, NC, USA

[6]Carolina Population Center, University of North Carolina, Chapel Hill, NC, USA

[7]Department of Sociology and Carolina Population Center, University of North Carolina, Chapel Hill, NC, USA

[8]Google, Inc., Mountain View, CA, USA

Corresponding author: Chao Wang (chao.wang@unc.edu)

Key Points:

- Quad polarized L-band UAVSAR and scattering mechanisms related polarimetric decomposition used here lead to high accuracy of flood extent mapping.
- The incidence angle normalization method used here effectively corrects the backscatter brightness that gradually decreases along the range direction.
- Dense UAVSAR time series reveal detailed flood extent variability, consistent with water height recorded at USGS gages.
-

Abstract

Extreme precipitation events are intensifying due to a warming climate, which, in some cases, is leading to increases in flooding. Detection of flood extent is essential for flood disaster management and prevention. However, it is challenging to delineate inundated areas through most publicly available optical and short-wavelength radar data, as neither can "see" through dense forest canopies. The 2018 Hurricane Florence produced heavy rainfall and subsequent record-setting riverine flooding in North Carolina, USA. NASA/JPL collected

daily high-resolution full-polarized L-band Uninhabited Aerial Vehicle Synthetic Aperture Radar (UAVSAR) data between September 18$^{th}$ and 23$^{rd}$. Here, we use UAVSAR data to construct a flood inundation detection framework through a combination of polarimetric decomposition methods and a Random Forest classifier. Validation of the established models with compiled ground references shows that the incorporation of linear polarizations with polarimetric decomposition and terrain variables significantly enhances the accuracy of inundation classification, and the Kappa statistic increases to 91.4% from 64.3% with linear polarizations alone. We show that floods receded faster near the upper reaches of the Neuse, Cape Fear, and Lumbee Rivers. Meanwhile, along the flat terrain close to the lower reaches of the Cape Fear River, the flood wave traveled downstream during the observation period, resulting in the flood extent expanding 16.1% during the observation period. In addition to revealing flood inundation changes spatially, flood maps such as those produced here have great potential for assessing flood damages, supporting disaster relief, and assisting hydrodynamic modeling to achieve flood-resilience goals.

## 1. Introduction

Floods are the most frequent, disastrous, and widespread natural hazards, accounting for more than 70% of hazard events occurring globally between 1994 and 2013 (UNISDR 2015). Between 1851 and 2017, more than three hundred hurricanes hit the U.S. East and Gulf coasts, causing massive damage, and upending the lives of millions (Song et al. 2018). Recent studies project that ongoing global climate change favors increased intensity of extreme weather events and a resulting increase of riverine and flash floods (Bender et al. 2010, Slater and Villarini 2016). Flood risk is especially increasing in low-lying coastal regions that are densely populated with some of the most valuable property worldwide (Kron 2013, Rueda et al. 2017, Qiang 2019). By 2050, worldwide annual losses due to flooding are projected to reach US $1 trillion for coastal cities (Hallegatte et al. 2013).

To achieve the goals of disaster risk reduction and sustainable development, governments and non-governmental organizations (NGOs) require access to near-real-time high-quality flood maps (Martinis et al. 2009, Schumann 2014). For instance, flood inventory maps are useful in supporting flood damage assessment (Chaabani et al. 2018), calibration and validation of flood inundation (i.e., hydraulic) models (Giustarini et al. 2015, Shin et al. 2020), climate change adaptation policies (e.g., flood risk mitigation planning) (Razavi et al. 2020), and the development of public disaster relief solutions (e.g., Flood Insurance Rate Maps) (Cian et al. 2018). The reliability of these maps directly affects the subsequent analysis and the effectiveness of relief policies (Hoch et al. 2019).

Airborne and spaceborne Earth observation platforms have revolutionized the monitoring of inundation dynamics during flood events (Dewan et al. 2006, Nateghi et al. 2016, Pradhan et al. 2016). Rapid progress has been made in flood detection algorithms that use optical images to assess flood events (Ban et al. 2017). Many early studies were based on relatively low spatial resolution

imagery ( 250 m), such as images from the Advanced Very High-Resolution Radiometer (AVHRR) and Moderate Resolution Imaging Spectrometer (MODIS) (Ali et al. 1989, Sanyal and Lu 2004, Brakenridge and Anderson 2006). These studies usually explore the advantage of high-frequency temporal measurements of inundation extent to partially compensate for limitations associated with cloud cover (Heimhuber et al. 2018). It is also common today to use optical imagery with a spatial resolution of 30 m or finer (e.g., Landsat and Sentinel 2 missions) for flood monitoring (Caballero et al. 2019). However, persistent cloud cover and long revisit time continue to limit the use of fine spatial resolution optical imagery for rapid response flood mapping during extreme weather events (Ban et al. 2017, Bioresita et al. 2018).

In contrast to optical imagery, synthetic aperture radar (SAR) systems characterize Earth's surface independent of weather conditions (Smith 1997). Due to high radar reflectivity differences between land and water associated with water's high dielectric constant, SAR has become particularly useful for mapping flood inundation (Hess et al. 2003, Brisco et al. 2009, Santoro and Wegmüller 2014). This is especially true in situations with persistent cloud cover, common during major flood events, when SAR provides a unique capacity for disaster monitoring (Twele et al. 2016, Ohki and Shimada 2018). The relevant scientific literature has grown rapidly over the last decade, coinciding more or less with recent launches of Earth-orbiting satellites carrying SAR instruments (e.g., PALSAR-2, Sentinel-1, Radarsat-2, TerraSAR-X, and CosmoSkyMed) (Clement et al. 2018, Huang et al. 2018, Benoudjit and Guida 2019, Cao et al. 2019). These SAR platforms have provided unprecedented L-, C-, and X-band observations of the Earth's land surface, all of which have been successfully used to monitor flood dynamics (Chapman et al. 2015, Bioresita et al. 2018, Shen et al. 2019b). It is worth noting that longer wavelength (e.g., L-band) SAR signals better penetrate vegetation canopy and undergo multiple scattering between the canopy, trunks, and forest floor or subcanopy inundation. Therefore, they are generally seen as superior to shorter wavelength SAR signals (e.g., X- or C-band) for flood detection (Hess et al. 1995, Jung et al. 2010, Zhang et al. 2016). In addition, fully polarimetric SAR (i.e., PolSAR) data allows the reconstruction of the complete scattering mechanisms from backscattered signals based on polarimetric decomposition methods, thus achieving an accurate detection of subcanopy inundation (White et al. 2014). However, most spaceborne SAR sensors have been operated to acquire data in single- or dual-polarization mode in nearly all observation configurations. And, due to long revisit times, sparseness of spaceborne SAR observations limits timely capture of flood dynamics (Clement et al. 2018). The dense time series quad-polarized L-band SAR imagery does not suffer from these limitations for flood extent mapping.

The Carolinas have suffered from devastating hurricanes frequently over recent years. In 2018, Hurricane Florence hovered over North Carolina for six days, delivering 25-35 inches of precipitation that led to catastrophic riverine flooding. Forty-four of North Carolina's 100 counties, home to an estimated 3.9 mil-

lion people, were declared federal disaster zones (Cooper 2018). The National Aeronautics and Space Administration (NASA) Uninhabited Aerial Vehicle Synthetic Aperture Radar (UAVSAR) platform, tasked by the Federal Emergency Management Agency (FEMA), collected substantial amounts of high-resolution quad-polarization airborne L-Band SAR imagery along the main rivers and their tributaries in the aftermath of the Hurricane Florence (September 17-23) (Lou et al. 2019). Because of the long, narrow shapes and low slopes of the watersheds in eastern North Carolina, the collected UAVSAR imagery coincided with extensive river flooding that occurred in the days after rainfall ceased. For example, flooding on the Lumbee River at Lumberton peaked on September $18^{\text{th}}$, several days after Florence made landfall, and did not drop below flood stage until October 6th. Therefore, the collected dense time series UAVSAR images provide a unique and valuable opportunity to construct a flood inundation detection framework to repeatedly map rapid changes in flood inundation extents, rather than sparse observations of flood inundation based on spaceborne instruments.

Using this repeat-pass daily UAVSAR data collected in the aftermath of Hurricane Florence, we develop detailed models to capture both open water and subcanopy inundation signals, with advantages in spatial resolution, temporal resolution, and accuracy compared to spaceborne optical or SAR data. To our knowledge, this is the first study to delineate daily inundation extents using multi-temporal quad-polarized L-band UAVSAR images during a flood. The specific objectives are to: i) map inundation extents spatially along floodplains of several big rivers of eastern North Carolina, and ii) analyze the rapidly changing flood inundation during these observation dates. This work can be extended to future near-real-time flood events response and disaster relief with the UAVSAR system, and can also help extend it to other areas when spaceborne quasi-polarized SAR systems become available on upcoming satellite missions.

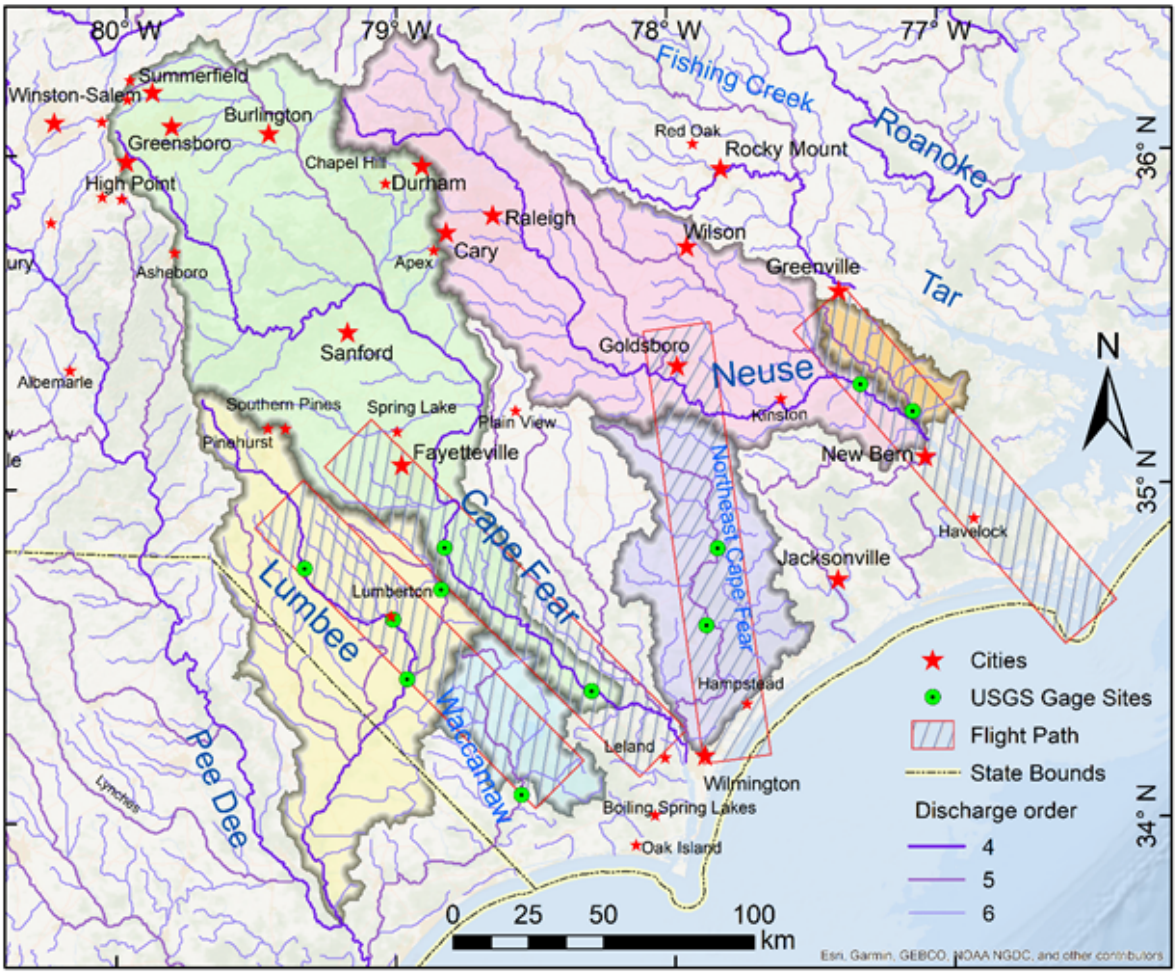


**Figure 1.** Map of four UAVSAR flight lines acquired along the Lower Neuse, Lower Cape Fear, and Lumbee Rivers of North Carolina during the record-breaking floods of September 2018 (Discharge order refers to the Backbone discharge order following the definition from Grill et al. (2019), and 4 refers to 100 - 1,000 m3/s; 5 refers to 10 - 100 m3/s and 6 refers to 1 - 10 m3/s). USGS gage stations are shown only within the experimental flight lines.

1. **Study Area**

The study area is situated in eastern North Carolina's lower coastal plain (Fig. 1). Several rivers flow east and southeast across the coastal plain and into the Atlantic Ocean. The local landscape is characterized by a gently sloping terrain with the land cover dominated by cropland, forests, and coastal swampy wetlands. It belongs to a humid subtropical climate (Köppen Climate Classification) (Rubel and Kottek 2010). Specifically, the summer is hot and extremely humid,

and the winter is cool with occasional short bouts of cold weather. Rains occur throughout the year but the potential for extreme rainfall events varies seasonally. During the Atlantic hurricane season (June 1 to November 30), extreme rainfall events can occur due to tropical cyclones and their remnants, especially during the peak period from mid-August through mid-October, which can cause serious flood disasters (Sayemuzzaman and Jha 2014).

1. **Methodology**

   (a) Datasets

      i. UAVSAR fully polarimetric data

UAVSAR's (http://uavsar.jpl.nasa.gov/) fully polarimetric airborne L-band SAR system, flying onboard NASA Armstong's Gulfstream-III, imaged the Hurricane Florence impact area in North Carolina in response to the expected historic flooding; the instrument itself was operated by personnel from NASA's Jet Propulsion Laboratory, who later processed the raw signal data into SAR imagery (Hensley et al. 2008). The L-band UAVSAR is a highly sensitive left-looking SAR with the ability to repeat flight tracks to within 10 meters via a precision autopilot control system (Rosen et al. 2006). The radar imaging instrument collects data at an incidence angle range of 22°-67° spanning a 22 kilometers swath in the cross-track direction, and up to 300 km in the along-track direction. The UAVSAR products used in this study are the multi-looked ground range projected (GRD, equiangular) imagery. The pixel spacing is 0.2 arcsec, corresponding to about 6 meters by 5 meters at the latitude of 35° along the latitude and longitude directions, respectively.

In the week following Hurricane Florence (September 17-23, 2018), NASA collected UAVSAR images of eight flight lines covering several major rivers and their tributaries in eastern North Carolina, with each flight-line imaged two to five times during that time period (Lou et al. 2019). In this study, we focused on four flight lines (i.e., 13510, 31509, 32023, and 35303) (Fig. 1) with four or more observations between September 18$^{\text{th}}$ and September 23$^{\text{rd}}$, corresponding to the area covering the Neuse, Cape Fear, and Lumbee Rivers as well as their tributaries. The areas covered are indicated by the hatched polygons in Fig. 1 and in Table S1.

1. Ground references

Following a flood event, flood extent maps produced by disaster survey experts through visual interpretation and manual digitalization of high-resolution aerial photographs are often considered to be the most reliable reference data (Ohki and Shimada 2018). These flood extent maps are usually used to validate the accuracy of automated remotely sensed flood detection (Sanyal and Lu 2004). However, the production of this data is both costly and inefficient, consequently, its availability is limited.

In this study, to collect ground references, we manually digitized polygons representing different classes. To do so, we randomly generated 2000 points that

overlapped with the UAVSAR flight track covering the Neuse River basin. We combined these points with high-water marks (HWM, as a reference for inundated and non-inundated locations) collected from the field by the U.S. Geological Survey (USGS) and North Carolina Division of Emergency Management (NCDEM) (https://stn.wim.usgs.gov/STNDataPortal/), high-resolution aerial photography collected by the National Oceanic and Atmospheric Administration (NOAA) (https://storms.ngs.noaa.gov/storms/florence/index.html) during the period of flooding, and high-resolution satellite imagery from Google Earth Pro. By overlaying the randomly generated points with these flood-related datasets (such as HWM and aerial photography), we manually digitized polygons near each point and visually interpreted and labeled them in 9 different classes (Fig. S1a and Table S3), including open surface water, open herbaceous vegetation on flood waters, sparse trees in flood waters, inundation beneath forest, wet grassland (or unharvested cropland), dry grassland (or fallow cropland dominated by bare soil), grass-dominated mosaic landscape, tree-dominated mosaic landscape, and upland forest. After preparing the digitized reference polygons, we randomly generated reference sample points based on the area of the polygons. Specifically, we randomly generated 7 points per 0.1 ha for each polygon, except for polygons smaller than 0.1 ha, where 7 random points are taken.

1. Terrain variables and other auxiliary datasets

The digital elevation model (DEM) data used in this study was downloaded from North Carolina State University Libraries (Newcomb and Terziotti 2013). It was derived from LIDAR collected in 2000 with a grid size of 20 feet (about 6 meters). The floating-point elevation values have been retained, which can be especially significant for applications in low topography areas of eastern NC. The elevation data were projected and resampled to 5-meter using the default bilinear resampling method to efficiently match UAVSAR data, and then used to derive topography slope and aspect. These three terrain variables were then used as complementary input predictors for the inundation classification model in addition to the primary predictors derived from UAVSAR data, because terrain variables, as key auxiliary predictors, play important roles in determining the distributions of vegetation and water (Wang et al. 2016).

In addition, several auxiliary datasets were used in the post-classification processing, such as urban impervious surfaces and inundation binary raster layers. The urban impervious surfaces binary raster layer was derived from the National Land Cover Database (NLCD) (Yang et al. 2018) and used as a control layer to mask false positives classified as inundated forest.

Moreover, we acquired concurrent multisource inundation maps derived from Landsat-7/8, Sentinel-2, and Sentinel-1 satellite data (mostly acquired on September 18, 2018, see detailed description in Table S5 of the satellite images used). Specifically, we applied Otsu's method on the spectral water index calculated based on cloud-free optical images following previous studies (Yao et al. 2015, Yao et al. 2019). The Sentinel 1 inundation binary raster data were downloaded from the global flood archive

(http://floodobservatory.colorado.edu/Events/4676/GISData/Other/UCONN/) produced by the Dartmouth Flood Observatory at the University of Colorado generated by Shen et al. (2019a). We applied the Median summary on the multisource inundation scenes together to create a binary inundation raster, which we used as a control layer for excluding false positives classified as open water.

1. USGS gage height data and river network data

In general, the extent of inundation delineated from satellite-based analysis is correlated with corresponding flood hydrographs (Bhatt et al. 2016). To further examine the inundation dynamics, we also collected stream gage height data from the USGS National Water Information System. For each study flight line, there are 2-4 continuously operating streamflow gages managed by the USGS (Fig. 1 and Table S7). We compared the dynamics of inundation extent delineated from UAVSAR with the corresponding same-day observed gage height information.

We used the Hydrological data and maps based on SHuttle Elevation Derivatives at multiple Scales (HydroSHEDS) dataset as a rivers network baseline (Lehner et al. 2008). The river order refers to the backbone discharge order which is calculated based on the long-term average discharge in cubic meters per second using logarithmic progression (Grill et al. 2019).

1. UAVSAR Processing

We constructed a flood detection algorithm framework (Fig. 2) building on previous work by Atwood et al. (2012), including extraction of T3 coherency matrix elements, "Refined Lee Filter" speckle filtering, polarization orientation angle correction, polarimetric decomposition, radiometric terrain correction, radiometric normalization, and supervised classification. The basic processing flow and the auxiliary data sets used are illustrated in Fig. 2. The workflow includes three major components. The processing steps in the pink box were carried out using the European Space Agency (ESA) PolSARpro v6.2 software package (Pottier et al, 2009) through custom python batch scripts. The steps in the light yellow and light blue boxes were implemented in the Google Earth Engine (GEE) platform using the python (v3.7.3) API (v0.1.200) because it provides online cloud computing tools and a flexible interactive development environment, facilitating easy sharing and reproducibility (Gorelick et al. 2017). These steps include radiometric terrain correction, radiometric normalization, and supervised classification modules.

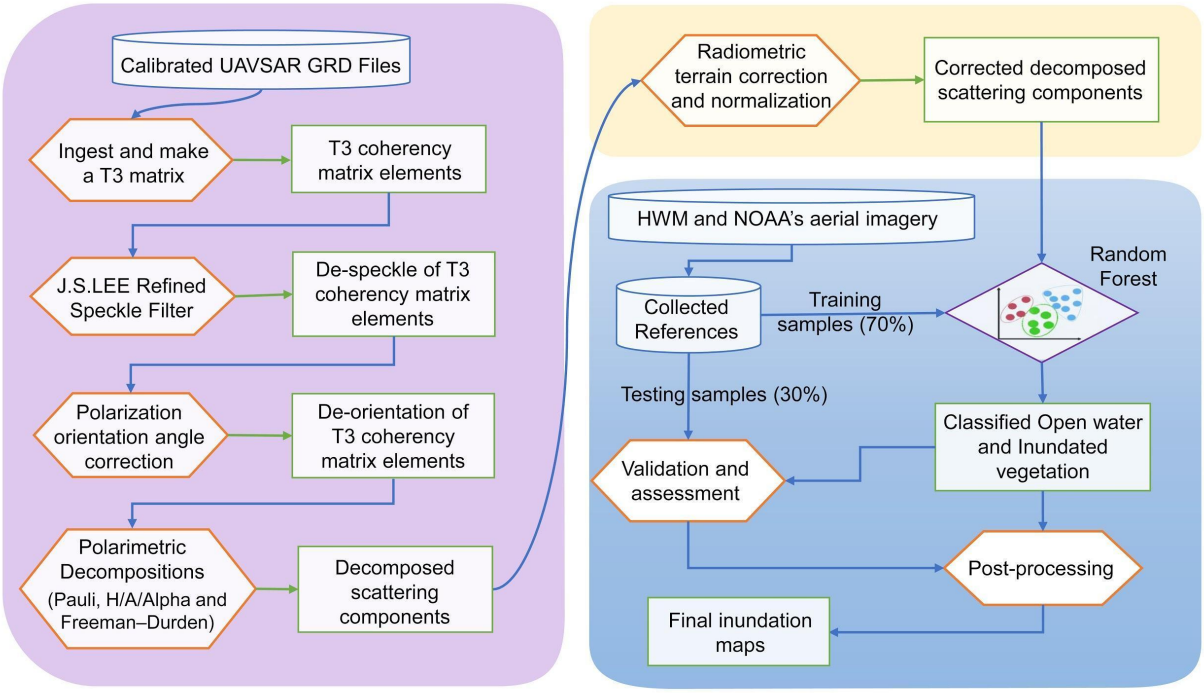


**Figure 2.** The proposed framework for flood inundation mapping from UAVSAR imagery (GRD refers to ground range projected UAVSAR data; T3 refers to coherency matrix derived from quad-polarized SAR data; Pauli, H/A/Alpha, and Freeman-Durden refer to three decomposition methods used here; HWM refers to high-water marks collected by the USGS and NCDEM; the steps in the pink box were carried out via the PolSARpro v6.2 software package; the steps in both yellow and blue boxes were implemented on the GEE platform; the steps in the light blue box make up the supervised classification module.)

1. Polarimetric de-speckling and de-orientation

Speckles appearing in SAR images are caused by the coherent interference of waves reflected from many elementary scatters (Lee et al. 1999). The de-speckling of PolSAR can dramatically boost the performance of image classification (Medasani and Reddy 2018). Here, we adopted the "Refined Lee Filter" speckle filtering method with a $3 \times 3$ window based on a tradeoff between spatial resolution and flood detection accuracy discussed in previous studies (Martinis and Rieke 2015, Ohki et al. 2019). This speckle filtering technique allows us to filter polarimetric data in a fast and simple way while avoiding additional coupling (or cross-talk) between the polarimetric channels (Lee et al. 1999).

In addition to de-speckling, we applied the "Polarization Orientation Compen-

sation" method to perform de-orientation for all UAVSAR images. Without de-orientation, the scattering mechanism may be misjudged in the PolSAR target decomposition step, and may thus lead to overestimation of the volume scattering component induced by topographical slopes (Lee and Ainsworth 2010, Atwood et al. 2012).

1. Polarimetric Decomposition

Since polarimetric information is sensitive to the geometric structure and physical characteristics of the target, to uncover its physical scattering mechanism, a measured polarimetric matrix can be decomposed into a summation of several dominant scattering mechanisms. Here, to explore the contribution of different physical scattering components derived from PolSAR data in the flood detection model, we adopted three different types of decomposition methods, including Pauli decomposition (PD), Freeman–Durden decomposition (FDD), and H/A/Alpha decomposition (also known as Cloude-Pottier decomposition, CPD) methods (see Methods in Supporting Information for details) (Qi et al. 2012, Freeman and Durden 1998, Cloude and Pottier 1997). As a result, we derived 10 decomposed polarimetric parameters from each UAVSAR dataset, consisting of three PD parameters, three FDD parameters, and four CPD parameters.

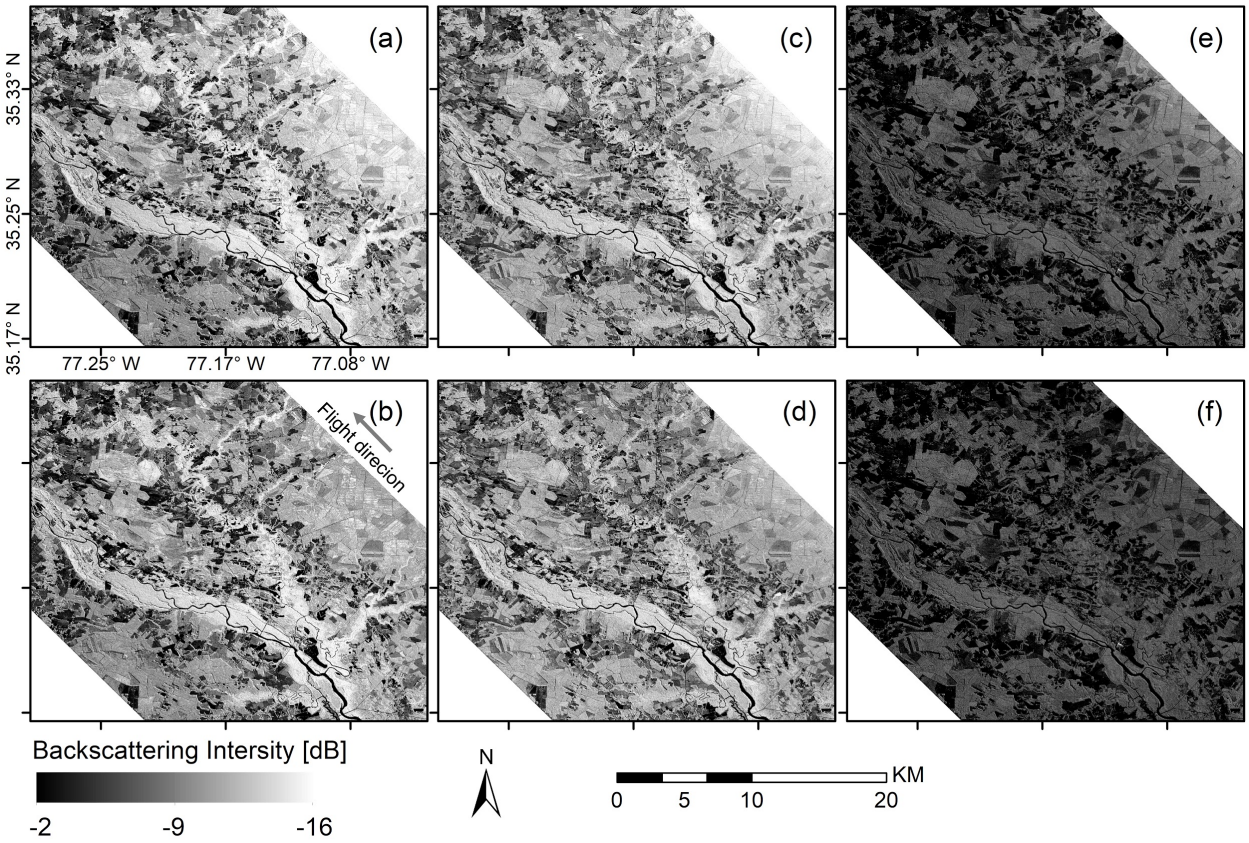


**Figure 3.** UAVSAR polarization intensity GRD images of the Neuse River Flightline on September 18$^{th}$ before and after radiometric normalization at the Neuse River basin near Vanceboro, Craven County, NC. ((**a**), (**c**), and (**e**) refer to the uncorrected HH, VV, and HV image; (**b**), (**d**), and (**f**) refer to the normalized HH, VV, and HV image with Eq. (3), the near- to far-range (i.e., from right upper to left bottom) corresponding to incidence angle from about 20° to 70°).

1. Polarization terrain correction and normalization

To correct for topographic effects, we applied the widely used two-stage semi-empirical terrain correction model proposed by Hoekman and Reiche (2015). Since our study area is topographically flat with dense forests but few open areas, the first stage of the model was sufficient to remove most of the topographic effects (Simard et al. 2016).

In addition to topographic effects, the backscatter intensity image shows a clear illumination gradient (e.g., Fig. 3a, c, and e) along the span with increasing incidence angle from near to far range due to the side-looking geometry config-

uration of UAVSAR (Ulaby et al. 1986). In this study, we applied radiometric normalization following Zhang et al. (2017) to correct all UAVSAR polarimetric parameters to the reference incidence angle for any given incidence angle (see Methods in Supporting Information for details). In addition, to make data in different flight lines comparable, the same reference incidence angle (57 ° equals 180 divided by PI) was adopted in the correction of all UAVSAR flight lines. It should be noted that the normalization procedure here just scales UAVSAR backscattered intensities at different incidence angles to the same intensity of backscattering at the incidence angle of 57 °, but it does not correct sensitivity of signal to be the same as observed at 57 °. The results that follow are not sensitive to the choice of reference incidence angle in this step.

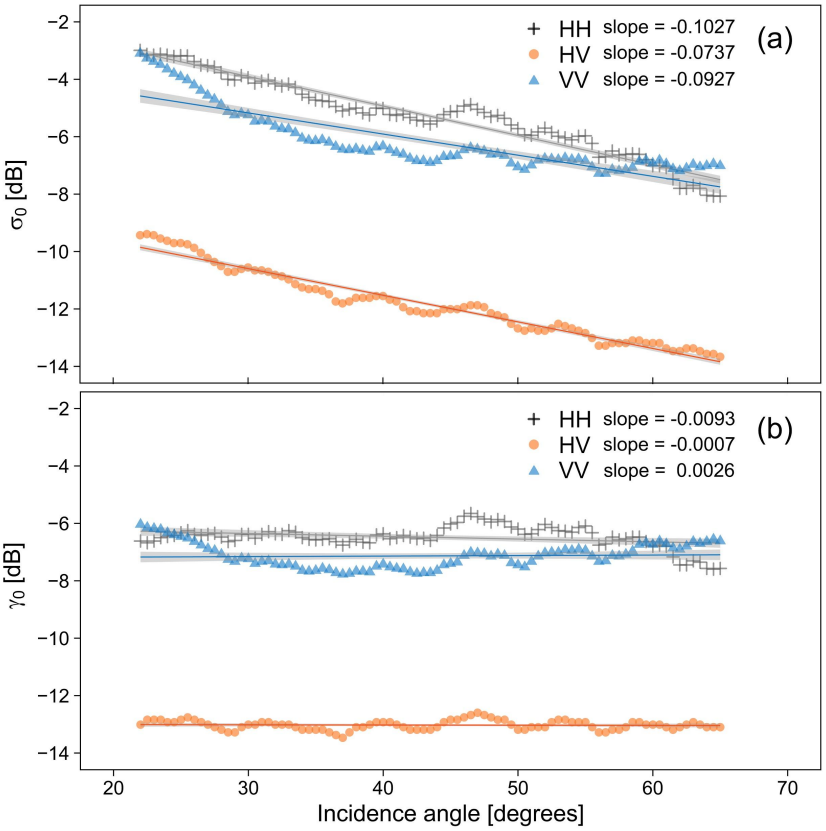


**Figure 4.** The mean of radar backscattering (dB) intensities versus incidence angle along radar range of the Neuse River Flightline on September 18$^{th}$: Upper panel (**a**) is the uncorrected data, and the bottom panel (**b**) shows results normalized with Eq. (3). Straight lines represent linear trends between backscattering intensities and incidence angle using best-fit regression and transparent shades illustrate 95% confidence intervals.

To evaluate the effectiveness of the correction, we selected four scenes of the flight track covering the Neuse River basin, spanning approximately 130 km from the Cape Lookout National Seashore in the southeast to the city of Greenville in the northwest. Along the cross-range direction, we extracted range profiles of averaged backscattering intensities. Fig. 4a presents the extracted range profiles and the corresponding linear regressions of one flight track scene (i.e., September $18^{th}$, Flightline ID "neuser_32023_18065_002_180918_L090") in HH, VV, and HV polarizations, which shows the general decrease in backscatter intensity with incidence angle. It is thus important to flatten the observed L-band backscatter along incidence angles to get consistent and comparable values for all incidence angles. In this study, after deriving the corresponding parameters for each scene (e.g., Table S2), we have successfully flattened the gradient of backscattering intensity along incidence angle (e.g., Fig. 4b and Fig. 3b, d, and f), which helps to accurately classify flood inundation then. Note that due to the spatial averaging discussed in the preceding section, we ignored the effects of speckle, geometrical shifts, and other disturbance factors associated with the UAVSAR data. The subtle, nonlinear variations with incidence angle in Fig. 4a and b are mostly caused by small differences in average land cover types perpendicular to the range direction.

1. Image classification using a Random Forest (RF) model

For training and validating classification models, we randomly split ground references into training (70% of each type) and testing (the remaining 30% of each type) datasets. During this step, we limited testing samples to be 2 UAVSAR-pixels (about 10 m) apart from the nearest training samples to avoid validation samples from identical or adjacent pixels, which ensures the generalizability of the subsequently trained models. This resulted in 12,607 training samples and 2,855 testing samples. We applied a Random Forest (RF) classifier on the training dataset to construct flood inundation classification models because the RF classifier is robust to the training datasets without making any distribution assumptions of the training data.

Here, we established three classification models using three combinations of input variables to explore the contributions of different sets of variables in the flood inundation detection framework. These three models are C1, using linear polarizations only (HH, HV, VV, and HH/VV); C2, using linear polarizations and polarimetric decomposition parameters; and C3, using linear polarizations, polarimetric decomposition and topographic variables. We considered the C1 model as the baseline model because, in most flood detection studies, linear polarizations have commonly been used, since most spaceborne SARs acquire data in single- or dual-polarization mode (Hess et al. 2003, Chapman et al. 2015). With the polarimetric decomposed variables added, the C2 model leverages the scattering mechanisms of inundated targets to generate more accurate flood inundation maps than what has been studied in-depth in previous studies (Ohki and Shimada 2018, Clement et al. 2018).

To quantify accuracy of each model, we validated the classification models

against the testing dataset by calculating producer's accuracy (complement of the Omission Error), user's accuracy (complement of the Commission Error), overall classification accuracy, and Kappa statistics. The original categories of the ground reference samples were reclassified into open surface water (WATR), inundation beneath forest (IBFC), grassland (GRAS), and forest (FORS) to simplify the accuracy analysis between categories that are most critical for understanding flood characteristics (Table S3).

To assess the importance of input variables in the model, we applied the Boruta algorithm with the 'Boruta' R package, which provides unbiased evaluation via an iteration process (Kursa and Rudnicki 2010). The experimental results (Fig. S2c) indicated that all input variables used in this study are detected as strongly relevant to the flood inundation classification, while the role of most polarimetric parameters from both CPD and FDD were superior to linear polarizations in the classification model.

Based on previous studies (Wang et al. 2015, Wang et al. 2017), we tuned the number of trees (NumTrees), the number of variables per split (NumSplit), and the minimum terminal node (Node) for the RF classification model, identifying the point at which errors stabilized. NumTrees, NumSplit, and Node were set as 800, 8, and 1 to optimize overall accuracy and efficiency (Fig. S2a and b). The well-trained RF model was subsequently used to produce flood inundation maps of daily repeat-pass UAVSAR scenes on different flight tracks between September $18^{\text{th}}$ and $23^{\text{rd}}$.

1. Classification postprocessing

Despite attempts to obtain the best possible results when performing image classification, the results of the initial classification, although good, were far from perfect regarding the salt and pepper effect. To get rid of these effects, post-processing is a very important step to generate thematic maps. In this study, we performed postprocessing procedures on open water and inundated vegetation separately, and then combined them together as the final inundation extent.

For the open water layer, some non-water pixels may also have lower L-band SAR backscatter values (e.g., man-made flat surfaces and bare soil fields), and therefore be confused with water pixels. We applied an exclusion layer of non-inundation based on the synthesized inundation raster data described in section 3.1.3C to limit commission errors.

For the inundated vegetation layer, walls of buildings in urbanized areas can cause similar double bounce effects as inundated vegetation. To remedy this, we exclude developed areas from the inundated vegetation layer based on the raster layer of urban impervious surfaces described in section 3.1.3C. In addition, linear backscatter enhancements (i.e., double bounce effects) also show in UAVSAR data depending on their geometry (e.g., forest edges oriented parallel to the flight track), resulting in some non-inundated pixels being misclassified as flooded forest (Chapman et al. 2015). These errors can be reduced using

morphological operations (Fig. S3). Here, we applied an alternating sequential filter (Soille and Pesaresi 2002) on the flooded vegetation layer with a closing (i.e., a dilation operation followed by an erosion operation) with a 2-pixel radius (i.e., ~10 meters) kernel and then a majority filter with a 1-pixel radius kernel to smooth the boundaries of detected flood patches, and finally an opening filter (i.e., the inverse of a closing filter) with a 2-pixel radius kernel to fill small holes in the flooded vegetation layer (Fig. S3a and b) and filter out linear false positives and other isolated flood objects which tend to appear as noise (Fig. S3c and d).

After producing the inundated layer by combining the open surface water and flooded forest layers together, we applied a second set of opening/closing filters to fill holes in the continuous flooded region and further exclude salt-and-pepper noise but with the kernel size of 4-pixel radius (i.e., ~20 meters) to keep a minimum mapping unit of 40 by 40 meters as a constraint. After classification post-processing, we also evaluated the quality of the final flood inundation extent products (i.e., inundated, or non-inundated binary classes) based on the testing datasets (reclassified as binary classes, see Table S6).

**Table 1**. Confusion matrices and accuracies for the three flood inundation classification models (i.e., C1, linear polarizations; C2, linear polarizations with added polarimetric parameters; and C3: the same variables as C2 but with added terrain variables). WATR, open surface water, open herbaceous vegetation on flooded water, and sparse tree trunks on flooded water; IBFC, inundation beneath forest canopy; GRAS, wet grassland, dry grassland, fallow cropland, and herbaceous-dominated classes; FORS, upland forest and dry tree-dominated mosaic landscape. The columns are the references, and the rows are the predicted classifications. UA, user's accuracy; PA, producer's accuracy, overall accuracy, and kappa coefficient.

| | **WATR** | **IBFC** | **GRAS** | **FOR** |
|---|---|---|---|---|
| **C1: Only polarization variables (HH, VV, HV, and HH/VV)** | | | | |
| **WATR** | 551 | 3 | 171 | 3 |
| **IBFC** | 10 | 290 | 23 | 100 |
| **GRAS** | 183 | 41 | 1055 | 40 |
| **FORS** | 19 | 64 | 56 | 246 |
| ***Sum*** | 763 | 398 | 1305 | 389 |
| ***PA (%)*** | 72.21% | 72.86% | 80.84% | 63.24% |
| Average PA=72.3%, Average UA=72.0%, OA=75.0%, Kappa=64.3% | | | | |
| **C2: Addition of decomposition variables** | | | | |
| **WATR** | 638 | 5 | 88 | 0 |
| **IBFC** | 16 | 370 | 0 | 33 |
| **GRAS** | 102 | 2 | 1201 | 19 |
| **FORS** | 7 | 21 | 16 | 337 |
| ***Sum*** | 763 | 398 | 1305 | 389 |
| ***PA (%)*** | 83.62% | 92.96% | 92.03% | 86.63% |
| Average PA=88.8%, Average UA=88.7%, OA=89.2%, Kappa=84.5% | | | | |

| | | | | |
|---|---|---|---|---|
| **C3: Addition of decomposition and terrain variables** | | | | |
| **WATR** | 690 | 1 | 49 | 0 |
| **IBFC** | 20 | 387 | 5 | 17 |
| **GRAS** | 51 | 3 | 1250 | 15 |
| **FORS** | 2 | 7 | 1 | 357 |
| ***Sum*** | 763 | 398 | 1305 | 389 |
| ***PA (%)*** | 90.43% | 97.24% | 95.79% | 91.77% |
| Average PA=93.8%, Average UA=93.9%, OA=94.0%, Kappa=91.4% | | | | |

1. **Results**

(a) Flood inundation classification accuracy

The base model (i.e. model C1 in Table 1) with only linear polarizations achieved a low overall accuracy (OA- 75.0%) and Kappa statistic (64.3%). The incorporation of polarimetric decomposition parameters to the base model substantially enhanced the classification of all the class types with overall accuracy and Kappa statistic increased by 14.2% and 20.2%, respectively (i.e., the model C2 in Table 1). Especially for IBFC and FORS classes, the omission errors declined from 27.1% to 7.0% and from 36.8% to 13.4%, respectively. Compared to the base model, the proportion of FORS references misclassified as IBFC was substantially reduced (from 25.7% to 8.5%), indicating the importance of polarimetric decomposition parameters, especially due to the enhanced double-bounce effect. Furthermore, the base model with the addition of polarimetric decomposition and terrain variables (i.e., C3 in Table 1) yielded the highest overall accuracy (94.0%) and Kappa statistic (91.4%). In particular, for WATR and IBFC, the C3 model reduced omission errors for these two classes from 28.8% to 9.6% and from 27.1% to 2.8%, respectively, relative to the base model. However, the main source of the errors observed in the C3 model from the confusion matrices can be attributed to the misclassification between WATR and GRAS (i.e., especially dry grassland, detailed in Table S4).

1. Space-Time Patterns in Flood Dynamics

The individual inundation extents derived from UAVSAR images using the above-mentioned method provided direct evidence of river flooding as well as inundation dynamics that occurred in the days following Hurricane Florence. Our results (i.e., Figs. 5, 6, 7, 8, S4, and S5) clearly indicated an identifiable change in inundation extents derived from repeat-pass UAVSAR during five days' observation (see Fig. S6 for the detailed locations of Figs. 5, 6, 7, 8, S4, and S5). To examine inundation dynamics, we analyzed the dynamics of inundation extent delineated from the airborne UAVSAR images with the same-day observed gage height. Specifically, we plotted the time-series inundation extent as points in the "inundation extent versus gage height" plot, calculated from our custom polygons within the adjacent watershed above each gage station.

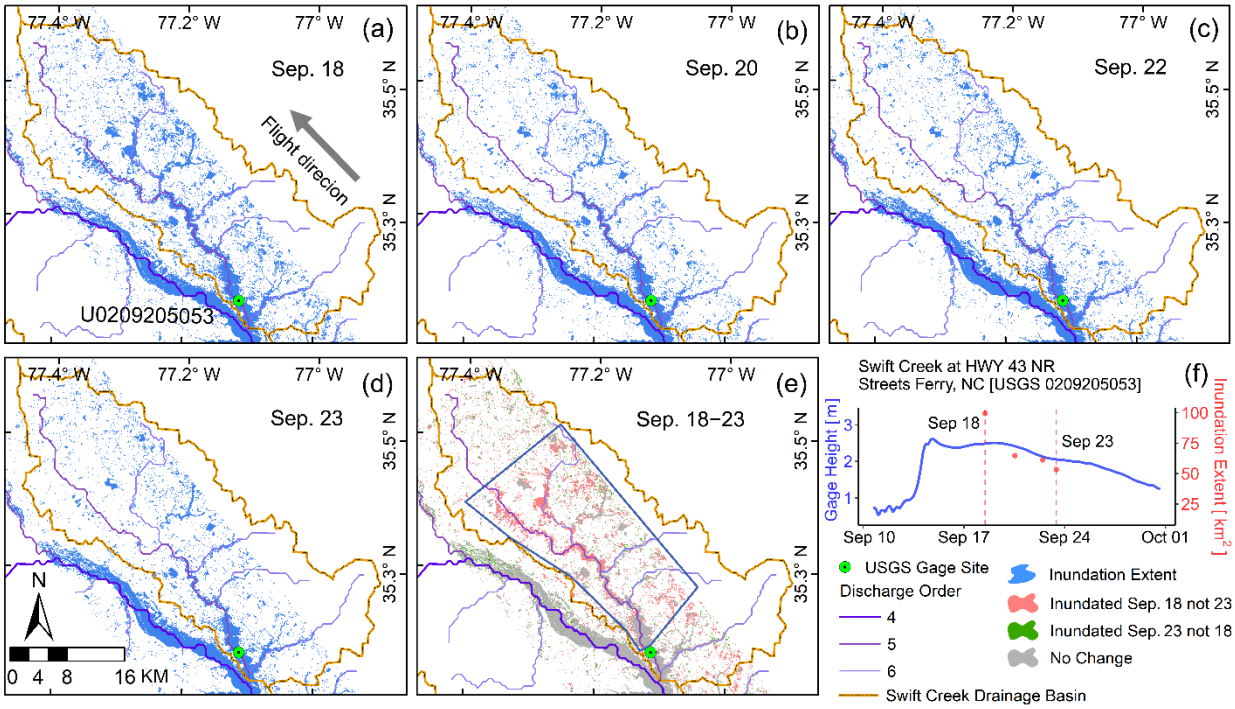


**Figure 5.** Inundation extent maps for the Swift Creek watershed, a tributary of the Neuse River, upstream of Streets Ferry gage station (USGS 0209205053). (**a**) 18 September 2018; (**b**) 20 September 2018; (**c**) 22 September 2018; (**d**) 23 September 2018; (**e**) difference between 18 and 23 September 2018, no changes are shown in gray, and the areas flooded only on 18 September in pink; areas flooded only on 23 September in green; (**f**) inundation extent versus gage height at the Streets Ferry, and the red dots series correspond to UAVSAR-derived inundation extents shown from (**a**) to (**d**), calculated over the blue polygon shown in (**e**). The red dashed lines are the time corresponding to the two UAVSAR observation times in (**e**).

During September 18-23, in the Swift Creek catchment, a tributary of the Neuse River (Fig. 1), inundation extent peaked on September 18$^{th}$ and then decreased over time (Fig. 5a-d), corresponding to the declining stage at the *Streets Ferry* gage station (USGS 0209205053, Fig. 5f). The reduction in inundation extent was about 52.6 km$^2$ (43.9%). We observed that the inundation extent decreased fastest between September 18$^{th}$ and 20$^{th}$ (Fig. 5a-b), and then it stabilized until the 23$^{rd}$ (Fig. 5c-d). In the change map showing in Fig. 5e, areas near the main channel with the river discharge order of 4 (i.e., 100 - 1,000 m$^3$/s) did not change significantly (shown in gray), while the flood extent near the tributaries with the discharge order of 5 (i.e., 10 - 100 m$^3$/s) declined substantially (shown in pink). There was almost no inundation expansion (shown in green) during the

study period. We also found that flood inundation changes in the Lumbee (Fig. S4) and Waccamaw (Fig. S5) River basins exhibited similar patterns of spatial variability.

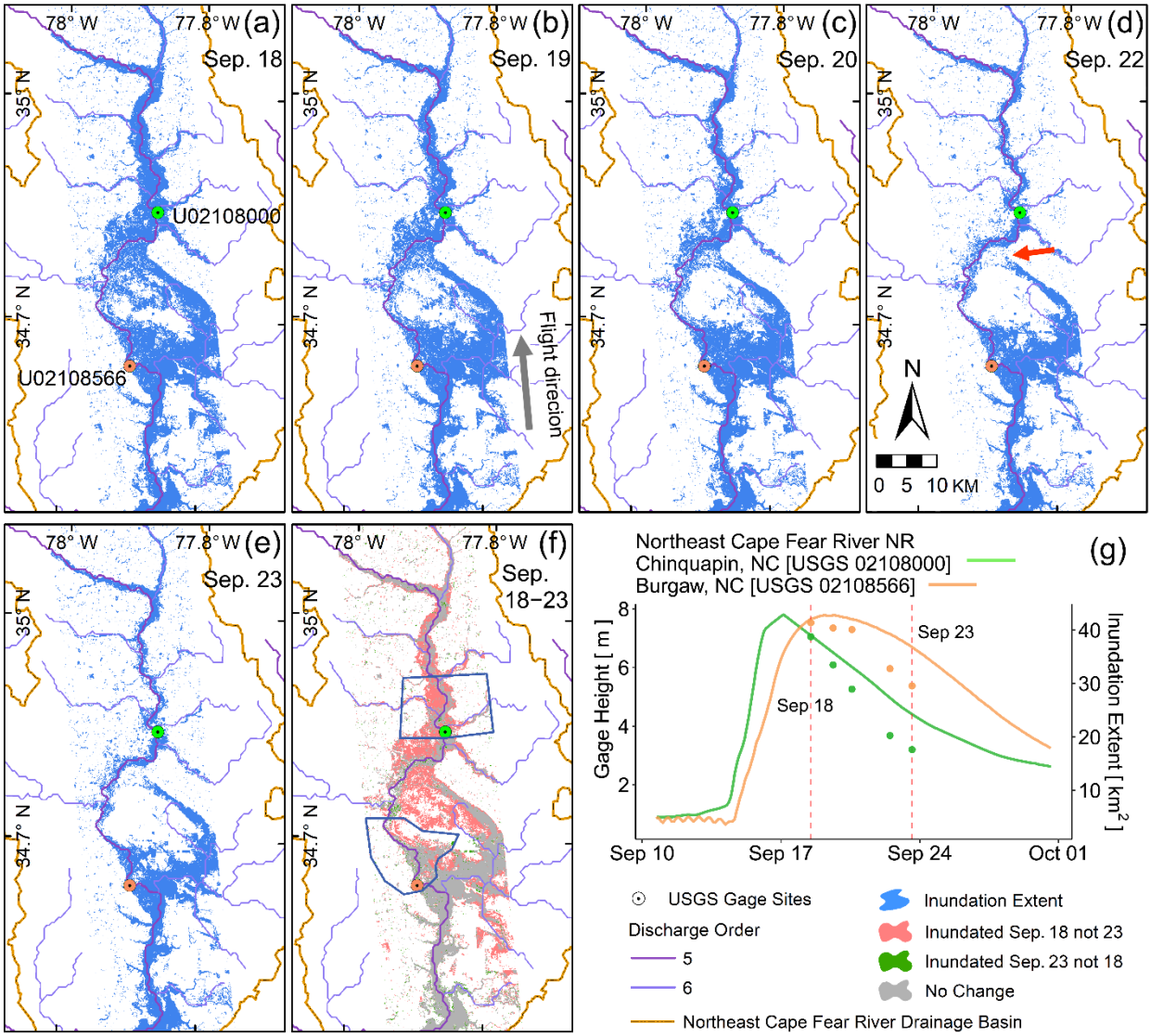


**Figure 6.** Inundation extent maps in the Northeast Cape Fear River Basin. (**a**) 18 September 2018; (**b**) 19 September 2018; (**c**) 20 September 2018; (**d**) 22 September 2018; (**e**) 23 September 2018; (**f**) difference between Sep 18 and 23, 2018, no changes are shown in gray, and the Areas flooded only on Sept 18 in pink; areas flooded only on Sept 23 in green; (**g**) Inundation extent versus gage height of the Chinquapin (USGS 02108000) and Burgaw (USGS 02108566) gage

stations, and the two colored dots series refer to the corresponding time-series UAVSAR observations from (**a**) to (**e**), calculated over two blue polygons shown in (**f**). The red dashed lines are the time corresponding to the two UAVSAR observation times in (**f**).

During these five observation dates, the Northeast Cape Fear River Basin witnessed remarkable inundation changes along main and tributary river floodplains (Fig. 6a-e). For the whole observation flight track of the Northeast Cape Fear River Basin, the inundation extent declined by 33.8% (211.4 $km^2$) during the five observation dates compared with the observed inundated extents on the first date (Fig. 6a and e). The extent of changes in inundation varies at different locations along the river channel (Fig. 6f). Specifically, in the drainage area above these two USGS gage stations, the inundation extent shrank by approximately 69.6 $km^2$ (-40.7%) and 150.0 $km^2$ ($-45.1\%$), respectively. We noticed that on the east side of the image downstream of the Chinquapin gage station (USGS 02108000), on September $18^{th}$ when the water surface elevation was just one day past the flow peak (Fig. 6g), a usually disconnected channel appeared to be connected, resulting in a temporarily altered network topology (Fig. 6a). As the inundation extent declined from September $18^{th}$ to September $22^{nd}$, this channel appeared disconnected again on September $22^{nd}$ (Fig. 6d, marked with a red arrow). Below the Chinquapin gage station, we also found that the flood inundation area was likely at its maximum on September $18^{th}$ and then decreased over time (Fig. 6a-f), as evidenced by the gage heights at the Burgaw station (Fig. 6g).

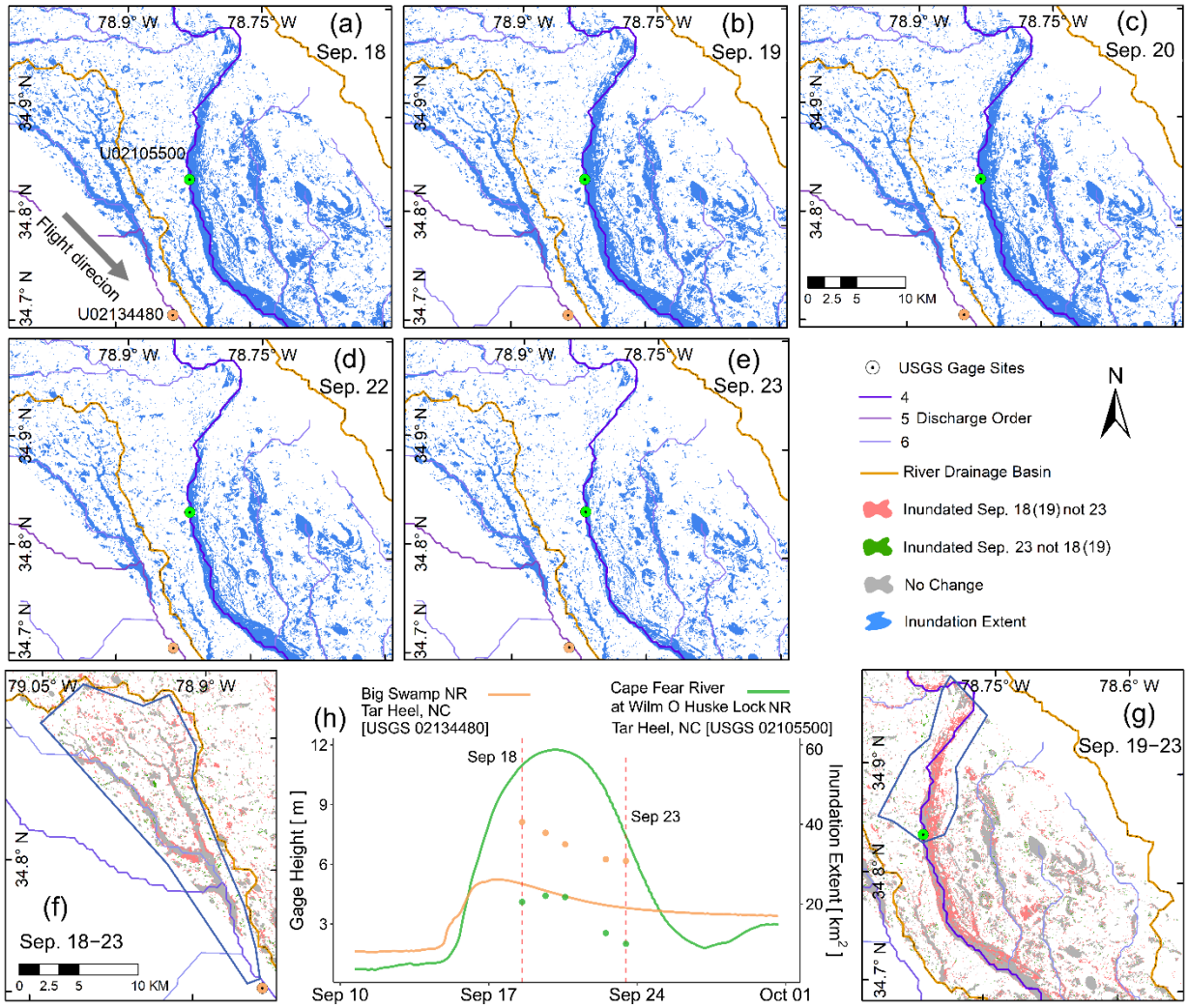


**Figure 7.** Inundation extent maps of the Lower Cape Fear River Basin near the Tar Heel gage station. (a) 18 September 2018; (b) 19 September 2018; (c) 20 September 2018; (d) 22 September 2018; (e) 23 September 2018; (f) difference between September 18 and 23, 2018 along the Big Swamp River; (g) difference between September 19 and 23, 2018 along the Lower Cape Fear River; (h) inundation extents versus gage heights, the center gage site (USGS 02105500) named Cape Fear River near Tar Heel, NC station (called the "Tar Heel station" herein) and the other gage site nearby (USGS 02134480) named Big Swamp near Tar Heel, NC station (called the "Big Swamp station" herein), and the two colored dots series refer to the corresponding UAVSAR observations near the two gage sites from (**a**) to (**e**), calculated over the blue polygon shown in (**f**) and (**g**). The red dashed lines are the time corresponding to the two UAVSAR

observation times in (**f**).

Fig. 7a-e shows inundation dynamics around the Lower Cape Fear River Basin near the Tar Heel gage station (USGS 02105500) as well as a small watershed above the Big Swamp gage station (USGS 02134480) on September $18^{\text{th}}$, $19^{\text{th}}$, $20^{\text{th}}$, $22^{\text{nd}}$, and $23^{\text{rd}}$. Dense time series observations during the flood events captured different peak times in these neighboring watersheds. Specifically, the inundation extent peaks along the Lower Cape Fear River above the Tar Heel gage on September $19^{\text{th}}$ (Fig. 7a-c and h, expanded 7.5% (1.5 $\text{km}^2$) from September $18^{\text{th}}$), while the inundation extent above the Big Swamp gage station has already passed its peak on September $18^{\text{th}}$ (Fig. 7a-b, and h). The time series of flood gage heights match the asynchronous dynamics in the inundation extent measurements between the two watersheds (Fig. 7h).

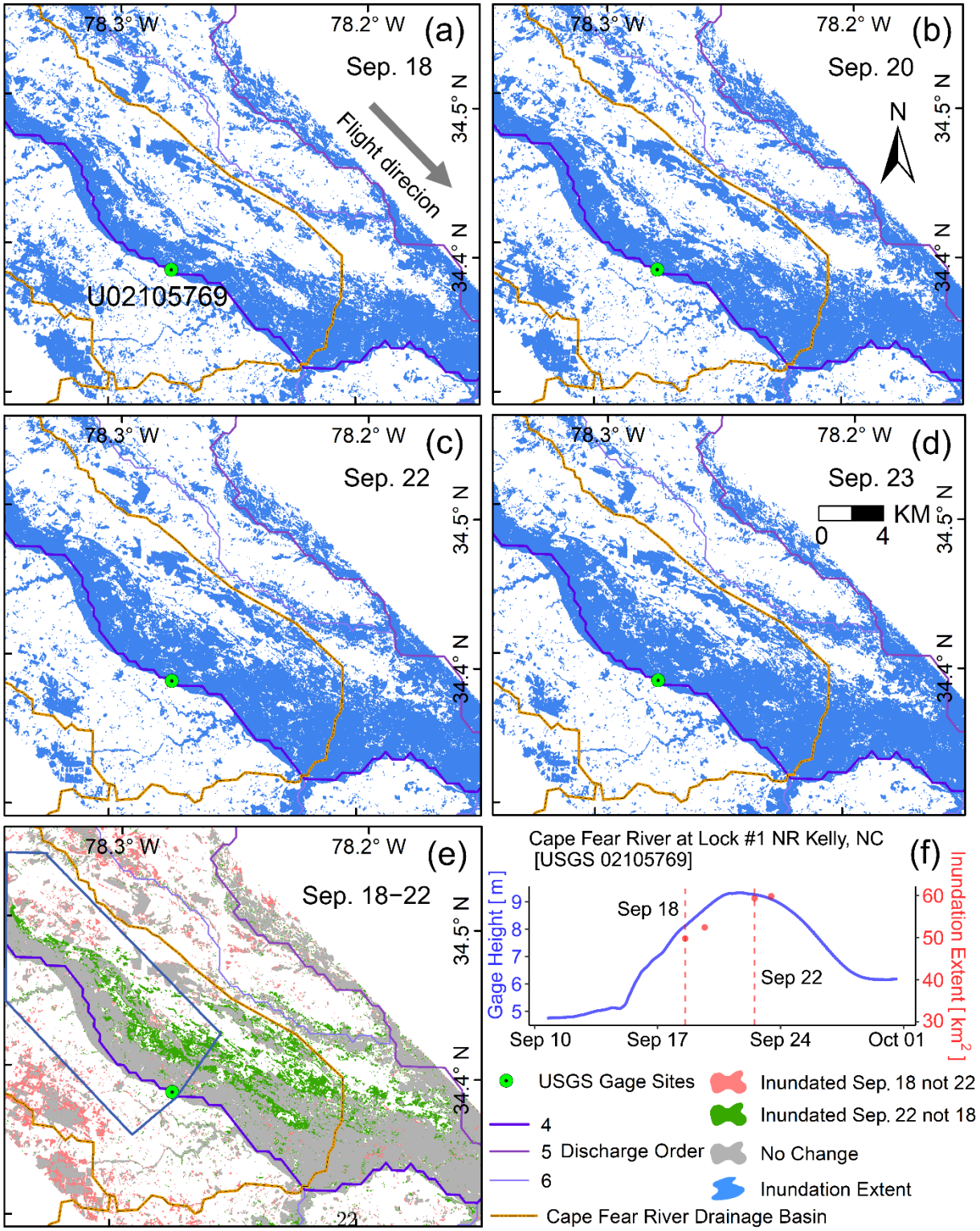
78.3° W
78.2° W
(a)
Sep. 18
Flight direcion
34.5° N
34.4° N
U02105769
(b)
Sep. 20
N
(c)
Sep. 22
(d)
Sep. 23
KM
0
4
(e)
Sep. 18−22
22
(f)
Cape Fear River at Lock #1 NR Kelly, NC
[USGS 02105769]
Gage Height [m]
Inundation Extent [km²]
Sep 18
Sep 22
Sep 10
Sep 17
Sep 24
Oct 01
USGS Gage Sites
4
5 Discharge Order
6
Cape Fear River Drainage Basin
Inundated Sep. 18 not 22
Inundated Sep. 22 not 18
No Change
Inundation Extent

**Figure 8.** Inundation extent maps in the Lower Cape Fear River Basin near Kelly, which is located in the downstream of Figure 7. (a) 18 September 2018; (b) 20 September 2018; (c) 22 September 2018; (d) 23 September 2018; (e) difference between Sep 18 and 22, 2018; (f) inundation extents versus gage heights from USGS 02105769, Cape Fear River near Kelly, NC. The red dots correspond to the time-series UAVSAR-derived inundation extents from September 18 to 23, 2018, calculated over the blue polygon in (**e**). The red dashed lines refer to the corresponding time of two UAVSAR observation time show in (**e**).

In addition to declining inundation extent along most river floodplains, flood inundation extents along the Lower Cape Fear River Basin near the Kelly gage station (USGS 02105769) expanded considerably several days after rainfall (i.e., September $19^{\text{th}}$, $20^{\text{th}}$, and $22^{\text{nd}}$, 2018, Fig. 8a-d). The inundation difference map between September $18^{\text{th}}$ and September $22^{\text{nd}}$ shown in Fig. 8e indicates that the inundated area expanded more than 9.5 $\text{km}^2$ (16.1%, calculated over the blue polygon within Lower Cape Fear River Basin) within four days near the main river channel above the Kelly gage station. This observed change in inundation extent is consistent with gage heights at the Kelly gage station (Fig. 8f).

Because of the long and narrow shape and flat slope of the Cape Fear River basin (Fig. 1), we observed an interesting phenomenon where flooding in the Lower Cape Fear River near Tar Heel (USGS 02105500) peaked on September $19^{\text{th}}$ (Fig. 7a and 7h), several days after Florence made landfall, and near Kelly station (USGS 02105769), further downstream, on September $22^{\text{nd}}$ (Fig. 8c and 8f). While this pattern is evident from the gage data alone, the remotely sensed imagery provides a comprehensive, near-daily picture of how inundation extent changes spatially in relation to the translation of the flood wave downstream.

Overall, in the aftermath of Hurricane Florence, rapid spatial changes in the flood extents of several major rivers in North Carolina, indicated that the floods receded fast in small tributaries of the Neuse, Cape Fear, Lumbee (Fig. S4), and Waccamaw (Fig. S5) Rivers and near the upper reaches of the Northeast Cape Fear River. Meanwhile, along the flat terrain close to the lower reaches of the Cape Fear River, the flood wave traveled downstream for four days after the cessation of rainfall (i.e., September $18^{\text{th}}$ - $22^{\text{nd}}$, 2018).

## 1. Discussion

Accurate and near-real-time monitoring of flood inundation extent is important for disaster response and immediate recovery in flood-prone lowland areas. In addition, understanding the extent of inundation and flood dynamics from past events, particularly in areas that are difficult to monitor, is critical for flood management and mitigation of future flood events. To the best of our knowledge, this is the first study to systematically examine temporal variations in hurricane-induced riverine floods using UAVSAR. Moreover, there has only been one previous study using UAVSAR data to estimate inundation extent after a hurricane event (Gebremichael et al. 2020); however, it was based on a single

day of data collection after Hurricane Harvey (2017). Thus, for the first time, we demonstrate UAVSAR's capacity to map temporal variations in flood inundation extents using daily time series of flood imagery. Based on the analysis of flooding dynamics and ground gage height data, we found that the delineated flood inundation extents in this study clearly captured the rapidly changing inundation extents following Hurricane Florence. The primary advances presented here can be divided into two categories: improvements in remote sensing methods and assessment of hydrologic relevance of UAVSAR data.

1. Advances in Remote Sensing Methods

In terms of data processing, based on the literature of multi-polarization SAR data, a logically clear processing framework has been developed in this study. UAVSAR collects data at incidence angles between about 20° and 70° from the near-range to the far-range, while larger incidence angles result in weaker contrast between flooded and non-flooded areas because of higher noise levels relative to lower backscatter intensity (Gan et al. 2012). It has been documented in previous studies (Townsend 2002, Schumann and Moller 2015, Manjusree et al. 2012) that considering scattering behaviors of floods at different incidence angles is critical to precisely detect flood extent. The normalization function adopted in this study effectively corrects the gradual decrease in brightness of the UAVSAR imagery along the range direction (Figs. 3 and 4), thus facilitating the subsequent accurate flood inundation classification of each UAVSAR scene. It is important to note that the normalization method used here would not solve the decreasing double bounce sensitivity as the incidence angle increases. Fortunately, the extracted inundation extents indicated that the detected inundation patches were clear and continuous even at the edge of the images (i.e., incidence angle more than 60° or less than 30°) (e.g., Figs. 5 and 7). However, the sensitivity of double bounce to incidence angle should be further investigated to ensure that inundated patches at the edges are as accurate as those at the incidence angles between 30° and 60°.

In addition to advanced processing methods, consistent with work by Ohki and Shimada (2018), the classification model based on linear polarizations alone in this study has been able to detect inundation/non-inundation but with relatively low accuracy (i.e., 64.3%). Our analysis shows that HH, VV, and HV polarizations have different contributions to the classification model, but have comparable importance scores (Fig. S2c). Our results are consistent with the SAR-based flood-related literature that collectively shows the use of HH is superior to VV polarization for flood area mapping (Ramsey III et al. 2013, Manavalan 2018). Because HH has a high radiometric dynamic range and tends to penetrate further into the subcanopy, while VV polarization appears to be more sensitive to rough water caused by turbulence or wind (Matgen et al. 2007). Schumann et al. (2007) suggested that in the absence of HH polarization data, the cross-polarization of VH (or HV) is the preferred choice over VV polarization for flood inundation mapping. However, this is not in line with our analysis on the importance of predictor variables. This difference may be due

to the use of different wavelengths (i.e., we used L-band, while Schumann et al. (2007) used C-band). In addition, unlike the study of Schumann et al. (2007) which only considered open flooded areas, our study also included inundated vegetation. While VH (or HV) polarization is not affected by double bounce effects and therefore cannot be used to detect inundated vegetation. Ahern et al. (2018) noted that the ratio of HH to VV appears to be a very good indicator for the areas dominated with inundated vegetation, especially in areas with high incidence angles that presented a strong Brewster angle effect (Thirion-Lefevre and Guinvarc'h 2018). In line with this finding, our study also suggested that the ratio of HH to VV plays an important role in the classification model and its importance ranking is superior to any polarization (Fig. S2c).

The addition of polarimetric decomposition features significantly enhanced the accuracy of our method for inundation classification (Table 1). Our results are consistent with the reports that scattering components from PolSAR were particularly advantageous for classifying inundated vegetation (Hong et al. 2015, Whelen and Siqueira 2017, Brown et al. 2016). In particular, the variable importance test using the Boruta algorithm highlighted that the decomposition variables derived from the CPD and FDD approaches play more important roles in the classification than the linear polarizations (Fig. S2c). In addition, the CPD-derived entropy and alpha angle features play a more important role than FDD-derived volume scattering and double-bounce scattering components in the classification. The knowledge gained here will support future airborne or spaceborne PolSAR missions for relevant hydrological applications such as flood extent monitoring and wetland vegetation mapping (Sokol et al. 2004, Hong et al. 2015, Lou et al. 2019).

The inclusion of terrain variables further improved the accuracy of the inundation classification model (Table 1), likely because topography affects distributions of both vegetation and surface water. This is especially true for elevation, which is the most important variable in the C3 classification model (Fig. S2c). In contrast, the slope and aspect parameters are not as important as elevation because of the relatively flat topography of the study area.

1. Advances in Flood Monitoring

Our results highlight that daily flood observations are a major improvement over the less frequent orbital data. Specifically, the dense time series of UAVSAR-derived flood inundation maps can provide detailed information even in highly forested and cloud-prone regions such as North Carolina where optical sensors often fail. In addition, our results reveal detailed variability in inundation extent in eastern North Carolina floodplains, consistent with water surface elevations recorded at USGS gages (Figs. 5, 6, 7, 8, S4, and S5). Specifically, our study reveals altered hydrologic flow pathways not apparent through gage data alone. For example, as illustrated by the red arrow in Fig. 6, a temporary hydrologic connection may have routed streamflow away from the main river channel (Fig. 6a), which fundamentally changed the river network topology and may have changed the geographic and temporal pattern of downstream flood hazard. This

result emphasizes the importance of dense time series flood observations from remotely sensed data, as it is presumably impossible to capture this phenomenon with gage data.

In addition, our method works particularly well in highly vegetated areas where few other methods can supply accurate inundation extent measurements but where floods still have implications on the natural environment and economy. For instance, extended periods of standing water after floods may severely affect forest health and increase potential vulnerability to insect pests and pathogens (Ranger et al. 2013). Based on these hydrologically relevant data and both statistical and hydrodynamic models, future studies could attempt to estimate inundation depth and duration, calculate flood recession rate, and assess flood-prone areas (Horritt et al. 2007, Schumann et al. 2010, Grimaldi et al. 2016). As extreme weather events like Florence may happen with increasing frequency and intensity under future climate conditions (Bender et al. 2010), a deep understanding of event evolution will help planning future flood mitigation measures and event management.

1. Limitations

Despite these interesting advances, this study has some limitations. First, the most robust validation data available to us, high-water marks, are not collected uniformly or consistently across our study area. In particular, flooded forest types were missing from the field survey data. Although the interpretation of NOAA high-resolution aerial photography and PolSAR decomposition data (Fig. S1b) in this study contributed to the collection of ground references of inundated forest type, it was dependent on experts' experience (Montgomery et al. 2019).

Another limitation is related to the sensitivity of the radar signal itself to flooded targets. Here, we acknowledge that the confusion of the backscattered signals between open surface water and smooth bare soil fields (such as dry grassland, fallow croplands or croplands that have recently been harvested) is an issue in this study, causing overestimation of inundation extents. This problem is in line with observations of Chapman et al. (2015) and Ohki et al. (2019) who reported that some non-flooded pixels were easily misclassified as water and occurred mainly in bare soil or low vegetation areas. In addition, based on daily L-band UAVSAR data, we did notice that backscatter intensity values of smooth fallow fields become progressively lower as the soil becomes drier after flood water receded. This may be because the reduction of moisture in the soil decreases the dielectric constant of the land surface and therefore reduces the amount of radar radiation reflected back, especially in dry soils with low dielectric constant and low radar reflectivity, making the backscattered intensity as low as that of open water (Sokol et al. 2004, Gallant et al. 2014). The fusion of open flood inundation data based on multi-source remotely sensed data substantially reduced the uncertainty of open surface water detection in the post-processing step. Thus, we strongly recommend fusion of optical and SAR remotely sensed data for open surface water detection.

In addition, the backscattered signal of the smooth artificial impermeable flat surface, such as that found in urban areas characterized by urban sprawl, also makes it difficult to distinguish from open surface water (Shen et al. 2019, Gebremichael et al., 2020). While we only used SAR collected during the flood event, it may be possible to correct this issue if pre-event data is also available. For example, Liu and Yamazaki (2018) used both pre-and co-event data to improve the accuracy of extracting flood extent.

Evaluation of the final inundation product after post-processing against the validation reference samples showed an overall accuracy reduction of 2.3% relative to the results of the inundation classification. For omission errors, the erosion operation did help to eliminate many linear-shape false positives at forest edges that occurred frequently in the landscapes of our study area (Fig. S3a and b). We note that some reference samples were collected in small, flooded ponds (Fig. S7a), and these small isolated water bodies have been filtered out because they do not meet the minimum map unit constraint (i.e., 40 by 40 meters). In some other cases, the generated reference samples appeared at the edge of the inundated area (Fig. S7b). The boundary smoothing procedure may incorrectly change inundated pixels at edges as non-inundated. For commission errors, the dilation operation may cause non-inundated pixels surrounded by inundated pixels to be mapped as inundated, such as the coastal wetland area of Fig. S7c and partially inundated cropland of Fig. S7d. In a word, post-processing procedures should be adjusted for specific applications, such as our riverine flooding monitoring application. If the study targets small ponds and water bodies, we recommend adapting post-processing procedures with caution.

Some minor limitations should also be noted in this study. Building walls in urban areas may cause foreshortening, layover, and double bounce effects (Cheng et al. 2013, Giustarini et al. 2013), so we masked out urban areas in this study because of their complex backscattering mechanisms and the small proportion of the landscape they represent in the images we studied. In addition, forest edges often exhibit clearly linear backscattering enhancements (i.e., double-bounce effects) in the UAVSAR images (when the forest edges are oriented parallel to the flight track) (Chapman et al. 2015), thus leading to misclassification as inundated forest (Fig. S3c). These effects can be eliminated to some extent with the erosion operation in post-processing steps.

In addition, for the limitations of monitoring spatial patterns of flood inundation, despite the fact that daily observations are a significant improvement over lower-frequency orbital data, daily observations may still miss high-water events if the high-water periods occur between flights. This situation is particularly likely to occur in areas where flood extent changes rapidly.

1. Perspectives for future research

Flood-related parameters, such as flood onset, maximum extent, and recession, are crucial for stakeholders to understand the impacts of extreme events (Sanyal and Lu 2004). Although there have been significant advances in satellite-based

flood monitoring in recent decades, low temporal frequency observations and persistent clouds have limited our ability to capture these parameters. For example, Clement et al. (2018) suggested that despite the 6-day revisit intervals of Sentinel-1, the sparseness of observations makes it difficult to interpret the data as an accurate representation of the flood time series. Management of future flood events will benefit from the joint SAR constellation of Sentinel-1, PALSAR-2, Radarsat-2, TerraSAR-X, and upcoming NISAR (i.e., NASA ISRO Synthetic Aperture Radar) mission satellites, and other commercial small satellites, such as ICEYE-X2 and Capella Space, thus providing denser time series flood observations.

The inundation extent mapping framework proposed in this study demonstrates that daily UAVSAR observations are capable of monitoring detailed spatially distributed flood dynamics. These flood inundation maps can serve as important validation datasets to reproduce riverine flood dynamics with hydraulic models for supporting flood-resilient communities (Grimaldi et al. 2016). For instance, dense time series of flood inundation maps can help address questions about optimal integration of remote sensing data with hydraulic models. Specifically, Horritt et al. (2007) reported that the observations acquired during the receding period were more effective at constraining model predictions of the 2000 Flood in the River Severn (UK) than the observations acquired at approximately peak flow. Data such as that used herein could allow further tests of this conclusion in a very different environment.

Additionally, our proposed inundation extent mapping framework demonstrates an excellent means to assist the forthcoming NISAR and SWOT (i.e., Surface Water Ocean Topography) missions during the calibration and validation (Cal/Val) experimental campaign phases. One common objective of these two missions is to measure inundation characteristics (such as inundation extent and water-surface elevation) of inland water bodies or wetland environments with fine spatial resolution and high temporal frequency (Biancamaria et al. 2016, Chapman et al. 2019). Precise and robust measurements of inundation extent derived from UAVSAR, concurrent with SWOT and NISAR overpasses, can complement expensive and time-limiting physical field-based surveys to validate SWOT- and NISAR-derived hydrological characteristics. Especially for SWOT during the 1-day revisit Cal/Val phase, it would be interesting to validate rapidly changing phenomena (e.g., flood events) by comparing with the results of concurrent daily UAVSAR data.

Our results suggested that based on polarimetric decomposition information, quad-pol UAVSAR data enabled the reconstruction of the complete scattering mechanisms rather than backscattering intensity information alone acquired by single- or dual-pol SAR sensors. While spaceborne L-band quad-pol SAR data is not freely accessible to the public yet, NISAR will generate quad-pol L-band SAR images over some targets, holding promise for mapping inundated vegetation with relatively high accuracy.

1. **Conclusion**

In this study, we proposed a flood extent detection framework for mapping inundation extent using daily, high-resolution (about 5-meter), full-polarized L-band UAVSAR data. This framework leverages many tools typically built for PolSAR processing, but it also includes new processing steps, such as the PolSAR normalization and supervised classification implemented on the cloud-computing infrastructure of GEE. We find that the framework proposed here can provide high-quality assessments of catastrophic floods in near-real-time based on UAVSAR data. Furthermore, the incorporation of linear polarizations with polarimetric decomposition (such as CPD and FDD) and terrain variables yielded the best flood extent detection model with a Kappa statistic of 91.4%, increasing by about 27.1% when compared to the baseline model (i.e., only linear polarization), which has been studied in-depth in previous studies. Our analysis showed that the dynamics of inundation extent delineated from daily UAVSAR data aligned with the same-day observed gage height in the aftermath of Hurricane Florence. Although flood wave patterns are evident from the gage data alone, the flood maps derived from UAVSAR data here provide a comprehensive, near-daily picture of how inundation extents vary spatially, e.g., inundation extents change locally relative to the translation of the flood wave downstream along the river channel.

In addition, the flood inundation maps produced here are particularly important for successfully filling in flood information gaps in eastern North Carolina, where dense vegetation may hamper flood inundation monitoring with optical data. For instance, they have great potential for assessing flood damages, supporting disaster relief, and assisting hydrodynamic modeling that supports planning for flood-resilient communities.

Since UAVSAR has become a well-established platform for L-band SAR data collection, the method presented in this study provides a way to timely and accurately generate inundation maps with fine spatial resolution and high temporal frequency. This approach provides accurate, dense time-series flood maps for future disaster response and recovery efforts and assists upcoming NISAR and SWOT missions during the calibration and validation (Cal/Val) experimental campaign phases, such as the ability to measure hydrological characteristics in wetland environments.

Acknowledgments and Data Availability Statement

This research was financially supported by the Dynamics of Extreme Events, People, and Places (DEEPP) project at University of North Carolina-Chapel Hill. The authors declare no conflicts of interest relevant to this study. The authors gratefully acknowledge those who designed, developed, and operate the Uninhabited Aerial Vehicle Synthetic Aperture Radar (UAVSAR). We would also like to thank PolSARpro and Google Earth Engine developers for their support and technical advice.

The derived flood inundation extent dataset associated with this study will be released at ORNL DAAC (current version dataset can be accessed through

this link: https://adminliveunc-my.sharepoint.com/:u:/r/personal/wayne128_ad_unc_edu/Documents/InundationExtent_Hurricane_Florence_UAVSAR_V2.0.zip?csf=1&web=1&e=ktx3Gg ). The UAVSAR polarimetric data used for this paper are available courtesy of NASA/JPL-Caltech (https://uavsar.jpl.nasa.gov/).

The code used for processing, mapping, and the analysis in this study can be found at https://github.com/waynechao128/FlorenceFlood_UAVSAR_Repo (this version is for review purpose and will be public released immediately after publishing in open-access repository such as Zenodo). All other data are also free to download with appropriate links in the analysis code.

References

Ahern, F., B. Brisco, K. Murnaghan, P. Lancaster, & D. K. Atwood. 2018. Insights Into Polarimetric Processing for Wetlands From Backscatter Modeling and Multi-Incidence Radarsat-2 Data. IEEE Journal of Selected Topics in Applied Earth Observations and Remote Sensing **11**:3040-3050.

Ali, A., D. A. Quadir, & O. K. Huh. 1989. Study of river flood hydrology in Bangladesh with AVHRR data. International Journal of Remote Sensing **10**:1873-1891.

Atwood, D. K., D. Small, & R. Gens. 2012. Improving PolSAR Land Cover Classification With Radiometric Correction of the Coherency Matrix. IEEE Journal of Selected Topics in Applied Earth Observations and Remote Sensing **5**:848-856.

Ban, H.-J., Y.-J. Kwon, H. Shin, H.-S. Ryu, & S. Hong. 2017. Flood monitoring using satellite-based RGB composite imagery and refractive index retrieval in visible and near-infrared bands. Remote Sensing **9**:313.

Bender, M. A., T. R. Knutson, R. E. Tuleya, J. J. Sirutis, G. A. Vecchi, S. T. Garner, & I. M. Held. 2010. Modeled impact of anthropogenic warming on the frequency of intense Atlantic hurricanes. Science **327**:454-458.

Benoudjit, A., & R. Guida. 2019. A Novel Fully Automated Mapping of the Flood Extent on SAR Images Using a Supervised Classifier. Remote Sensing **11**:779.

Bhatt, C., G. Rao, P. Diwakar, & V. Dadhwal. 2016. Development of flood inundation extent libraries over a range of potential flood levels: a practical framework for quick flood response. Geomatics, Natural Hazards and Risk **8**:384-401.

Biancamaria, S., D. P. Lettenmaier, & T. M. Pavelsky. 2016. The SWOT Mission and Its Capabilities for Land Hydrology. Surveys in Geophysics **37**:307-337.

Bioresita, F., A. Puissant, A. Stumpf, and J.-P. Malet. 2018. A Method for

Automatic and Rapid Mapping of Water Surfaces from Sentinel-1 Imagery. Remote Sensing **10**:217.

Bouvet, A., S. Mermoz, M. Ballère, T. Koleck, & T. Le Toan. 2018. Use of the SAR shadowing effect for deforestation detection with Sentinel-1 time series. Remote Sensing **10**:1250.

Brakenridge, R., & E. Anderson. 2006. MODIS-based flood detection, mapping and measurement: the potential for operational hydrological applications (pp. 1-12). Springer Netherlands, Dordrecht.

Brisco, B., N. Short, J. v. d. Sanden, R. Landry, & D. Raymond. 2009. A semi-automated tool for surface water mapping with RADARSAT-1. Canadian Journal of Remote Sensing **35**:336-344.

Brown, I., S. Mwansasu, & L.-O. Westerberg. 2016. L-Band Polarimetric Target Decomposition of Mangroves of the Rufiji Delta, Tanzania. Remote Sensing **8**:140.

Caballero, I., J. Ruiz, & G. Navarro. 2019. Sentinel-2 satellites provide near-real time evaluation of catastrophic floods in the west mediterranean. Water **11**:2499.

Cao, H., H. Zhang, C. Wang, & B. Zhang. 2019. Operational Flood Detection Using Sentinel-1 SAR Data over Large Areas. Water **11**:786.

Chaabani, C., M. Chini, R. Abdelfattah, R. Hostache, & K. Chokmani. 2018. Flood Mapping in a Complex Environment Using Bistatic TanDEM-X/TerraSAR-X InSAR Coherence. Remote Sensing **10**:1873.

Chapman, B., K. McDonald, M. Shimada, A. Rosenqvist, R. Schroeder, & L. Hess. 2015. Mapping Regional Inundation with Spaceborne L-Band SAR. Remote Sensing **7**:5440-5470.

Chapman, B., P. Siqueira, S. Saatchi, M. Simard, & J. Kellndorfer. 2019. Initial results from the 2019 NISAR Ecosystem Cal/Val Exercise in the SE USA. (pp. 8641-8644) IEEE International Geoscience and Remote Sensing Symposium (IGARSS 2019).

Cheng, X., W. Huang, & J. Gong. 2013. A decomposition-free scattering mechanism classification method for PolSAR images with Neumann's model. Remote Sensing Letters **4**:1176-1184.

Cian, F., M. Marconcini, & P. Ceccato. 2018. Normalized Difference Flood Index for rapid flood mapping: Taking advantage of EO big data. Remote Sensing of Environment **209**:712-730.

Clement, M. A., C. G. Kilsby, & P. Moore. 2018. Multi-temporal synthetic aperture radar flood mapping using change detection. Journal of Flood Risk Management **11**:152-168.

Cloude, S. R., & E. Pottier. 1997. An entropy based classification scheme for land applications of polarimetric SAR. IEEE Transactions on Geoscience and Remote Sensing **35**:68-78.

Cooper, R. 2018. Hurricane Florence recovery recommendations. North Carolina Emergency Management (NCEM).

Dewan, A. M., M. M. Islam, T. Kumamoto, & M. Nishigaki. 2006. Evaluating Flood Hazard for Land-Use Planning in Greater Dhaka of Bangladesh Using Remote Sensing and GIS Techniques. Water Resources Management **21**:1601-1612.

Freeman, A., & S. L. Durden. 1998. A three-component scattering model for polarimetric SAR data. IEEE Transactions on Geoscience and Remote Sensing **36**:963-973.

Furtado, L. F. d. A., T. S. F. Silva, & E. M. L. d. M. Novo. 2016. Dual-season and full-polarimetric C band SAR assessment for vegetation mapping in the Amazon várzea wetlands. Remote Sensing of Environment **174**:212-222.

Gallant, A., S. Kaya, L. White, B. Brisco, M. Roth, W. Sadinski, & J. Rover. 2014. Detecting Emergence, Growth, and Senescence of Wetland Vegetation with Polarimetric Synthetic Aperture Radar (SAR) Data. Water **6**:694-722.

Gan, T. Y., F. Zunic, C. C. Kuo, & T. Strobl. 2012. Flood mapping of Danube River at Romania using single and multi-date ERS2-SAR images. International Journal of Applied Earth Observation and Geoinformation **18**:69-81.

Gebremichael, E., A. L. Molthan, J. R. Bell, L. A. Schultz, & C. Hain. 2020. Flood Hazard and Risk Assessment of Extreme Weather Events Using Synthetic Aperture Radar and Auxiliary Data: A Case Study. Remote Sensing **12**:3588.

Giustarini, L., M. Chini, R. Hostache, F. Pappenberger, & P. Matgen. 2015. Flood hazard mapping combining hydrodynamic modeling and multi annual remote sensing data. Remote Sensing **7**:14200-14226.

Giustarini, L., R. Hostache, P. Matgen, G. J. Schumann, P. D. Bates, & D. C. Mason. 2013. A Change Detection Approach to Flood Mapping in Urban Areas Using TerraSAR-X. IEEE Transactions on Geoscience and Remote Sensing **51**:2417-2430.

Gorelick, N., M. Hancher, M. Dixon, S. Ilyushchenko, D. Thau, & R. Moore. 2017. Google Earth Engine: Planetary-scale geospatial analysis for everyone. Remote Sensing of Environment **202**:18-27.

Grill, G., B. Lehner, M. Thieme, B. Geenen, D. Tickner, F. Antonelli, S. Babu, P. Borrelli, L. Cheng, H. Crochetiere, H. Ehalt Macedo, R. Filgueiras, M. Goichot, J. Higgins, Z. Hogan, B. Lip, M. E. McClain, J. Meng, M. Mulligan, C. Nilsson, J. D. Olden, J. J. Opperman, P. Petry, C. Reidy Liermann, L. Sáenz, S. Salinas-Rodríguez, P. Schelle, R. J. P. Schmitt, J. Snider, F. Tan, K. Tockner, P. H.

Valdujo, A. van Soesbergen, & C. Zarfl. 2019. Mapping the world's free-flowing rivers. Nature **569**:215-221.

Grimaldi, S., Y. Li, V. R. Pauwels, & J. P. Walker. 2016. Remote sensing-derived water extent and level to constrain hydraulic flood forecasting models: Opportunities and challenges. Surveys in Geophysics **37**:977-1034.

Hallegatte, S., C. Green, R. J. Nicholls, & J. Corfee-Morlot. 2013. Future flood losses in major coastal cities. Nature Climate Change **3**:802-806.

Heimhuber, V., M. Tulbure, & M. Broich. 2018. Addressing spatio-temporal resolution constraints in Landsat and MODIS-based mapping of large-scale floodplain inundation dynamics. Remote Sensing of Environment **211**:307-320.

Hensley, S., K. Wheeler, G. Sadowy, C. Jones, S. Shaffer, H. Zebker, T. Miller, B. Heavey, E. Chuang, R. Chao, K. Vines, K. Nishimoto, J. Prater, B. Carrico, N. Chamberlain, J. Shimada, M. Simard, B. Chapman, R. Muellerschoen, C. Le, T. Michel, G. Hamilton, D. Robison, G. Neumann, R. Meyer, P. Smith, J. Granger, P. Rosen, D. Flower, & R. Smith. 2008. The UAVSAR instrument: Description and first results. Pages 1-6 *in* 2008 IEEE Radar Conference.

Hess, L. L., J. M. Melack, S. Filoso, & W. Yong. 1995. Delineation of inundated area and vegetation along the Amazon floodplain with the SIR-C synthetic aperture radar. IEEE Transactions on Geoscience and Remote Sensing **33**:896-904.

Hess, L. L., J. M. Melack, E. M. L. M. Novo, C. C. F. Barbosa, & M. Gastil. 2003. Dual-season mapping of wetland inundation and vegetation for the central Amazon basin. Remote Sensing of Environment **87**:404-428.

Hoch, J. M., D. Eilander, H. Ikeuchi, F. Baart, & H. C. Winsemius. 2019. Evaluating the impact of model complexity on flood wave propagation and inundation extent with a hydrologic-hydrodynamic model coupling framework. Natural Hazards and Earth System Sciences **19**:1723-1735.

Hoekman, D. H., & J. Reiche. 2015. Multi-model radiometric slope correction of SAR images of complex terrain using a two-stage semi-empirical approach. Remote Sensing of Environment **156**:1-10.

Hong, S.-H., H.-O. Kim, S. Wdowinski, & E. Feliciano. 2015. Evaluation of Polarimetric SAR Decomposition for Classifying Wetland Vegetation Types. Remote Sensing **7**:8563-8585.

Horritt, M. S., G. Di Baldassarre, P. D. Bates, & A. Brath. 2007. Comparing the performance of a 2-D finite element and a 2-D finite volume model of floodplain inundation using airborne SAR imagery. Hydrological Processes **21**:2745-2759.

Hosseiny, H., F. Nazari, V. Smith, & C. Nataraj. 2020. A framework for Modeling flood Depth Using a Hybrid of Hydraulics and Machine Learning. Scientific Reports **10**:1-14.

Hostache, R., P. Matgen, G. Schumann, C. Puech, L. Hoffmann, & L. Pfister. 2009. Water level estimation and reduction of hydraulic model calibration uncertainties using satellite SAR images of floods. IEEE Transactions on Geoscience and Remote Sensing **47**:431-441.

Huang, W., B. DeVries, C. Huang, M. Lang, J. Jones, I. Creed, & M. Carroll. 2018. Automated Extraction of Surface Water Extent from Sentinel-1 Data. Remote Sensing **10**:797.

Jung, H. C., J. Hamski, M. Durand, D. Alsdorf, F. Hossain, H. Lee, A. A. Hossain, K. Hasan, A. S. Khan, & A. Z. Hoque. 2010. Characterization of complex fluvial systems using remote sensing of spatial and temporal water level variations in the Amazon, Congo, and Brahmaputra Rivers. Earth Surface Processes and Landforms: The Journal of the British Geomorphological Research Group **35**:294-304.

Kron, W. 2013. Coasts: the high-risk areas of the world. Natural Hazards **66**:1363-1382.

Kursa, M. B., & W. R. Rudnicki. 2010. Feature selection with the Boruta package. J Stat Softw **36**:1-13.

Lee, J.-S., M. R. Grunes, & G. De Grandi. 1999. Polarimetric SAR speckle filtering and its implication for classification. IEEE Transactions on Geoscience and Remote Sensing **37**:2363-2373.

Lee, J.-S., & E. Pottier. 2009. Polarimetric radar imaging: from basics to applications. CRC press.

Lee, J., & T. L. Ainsworth. 2010. The effect of orientation angle compensation on coherency matrix and polarimetric target decompositions. IEEE Transactions on Geoscience and Remote Sensing **49**:53-64.

Lehner, B., K. Verdin, & A. Jarvis. 2008. New Global Hydrography Derived From Spaceborne Elevation Data. Eos, Transactions American Geophysical Union **89**:93-94.

Liu, W., & F. Yamazaki. 2018. Detection of inundation areas due to the 2015 Kanto and Tohoku torrential rain in Japan based on multi-temporal ALOS-2 imagery. Natural Hazards & Earth System Sciences **18**.

Lou, Y., S. Hensley, B. Chapman, B. Hawkins, C. Jones, P. Lundgren, T. Michel, R. Muellerschoen, N. Pinto, & Y. Zheng. 2019. Recent Airborne Sar Demonstrations for Monitoring and Assessment of Volcanic Lava Flow and Severe Flooding. Pages 9388-9390 *in* IGARSS 2019 - 2019 IEEE International Geoscience and Remote Sensing Symposium.

Manavalan, R. 2018. Review of synthetic aperture radar frequency, polarization, and incidence angle data for mapping the inundated regions. Journal of Applied Remote Sensing **12**:021501.

Manjusree, P., L. Prasanna Kumar, C. M. Bhatt, G. S. Rao, & V. Bhanumurthy. 2012. Optimization of threshold ranges for rapid flood inundation mapping by evaluating backscatter profiles of high incidence angle SAR images. International Journal of Disaster Risk Science **3**:113-122.

Martinis, S., & C. Rieke. 2015. Backscatter Analysis Using Multi-Temporal and Multi-Frequency SAR Data in the Context of Flood Mapping at River Saale, Germany. Remote Sensing **7**:7732-7752.

Martinis, S., A. Twele, & S. Voigt. 2009. Towards operational near real-time flood detection using a split-based automatic thresholding procedure on high resolution TerraSAR-X data. Nat. Hazards Earth Syst. Sci. **9**:303-314.

Matgen, P., G. Schumann, J. B. Henry, L. Hoffmann, & L. Pfister. 2007. Integration of SAR-derived river inundation areas, high-precision topographic data and a river flow model toward near real-time flood management. International Journal of Applied Earth Observation and Geoinformation **9**:247-263.

Medasani, S., & G. U. Reddy. 2018. Speckle Filtering and its Influence on the Decomposition and Classification of Hybrid Polarimetric Data of RISAT-1. Remote Sensing Applications: Society and Environment **10**:1-6.

Menges, C. H., J. J. Van Zyl, G. J. E. Hill, & W. Ahmad. 2001. A procedure for the correction of the effect of variation in incidence angle on AIRSAR data. International Journal of Remote Sensing **22**:829-841.

Montgomery, J., B. Brisco, L. Chasmer, K. Devito, D. Cobbaert, & C. Hopkinson. 2019. SAR and Lidar Temporal Data Fusion Approaches to Boreal Wetland Ecosystem Monitoring. Remote Sensing **11**:161.

Nateghi, R., J. D. Bricker, S. D. Guikema, & A. Bessho. 2016. Statistical Analysis of the Effectiveness of Seawalls and Coastal Forests in Mitigating Tsunami Impacts in Iwate and Miyagi Prefectures. PLoS One **11**:e0158375.

Newcomb, D., & S. Terziotti. 2013. A seamless aggregation of the tiled 20 ft elevation DEM tiles generated by the North Carolina Floodplain Mapping Project.*in* U. S. F. a. W. S. a. U. S. G. Survey, editor. NC State University Libraries, https://www.lib.ncsu.edu/gis/elevation.

Ohki, M., & M. Shimada. 2018. Flood-Area Detection Using Palsar-2 Data for Heavy Rainfall Disasters in Japan. Pages 8777-8780 *in* IGARSS 2018 - 2018 IEEE International Geoscience and Remote Sensing Symposium.

Ohki, M., T. Tadono, T. Itoh, K. Ishii, T. Yamanokuchi, M. Watanabe, & M. Shimada. 2019. Flood Area Detection Using PALSAR-2 Amplitude and Coherence Data: The Case of the 2015 Heavy Rainfall in Japan. IEEE Journal of Selected Topics in Applied Earth Observations and Remote Sensing **12**:2288-2298.

Pottier, E., et al., "Overview of the PolSARpro V4.0 software. the open source toolbox for polarimetric and interferometric polarimetric SAR data

processing," 2009 IEEE International Geoscience and Remote Sensing Symposium, Cape Town, South Africa, 2009, pp. IV-936-IV-939, doi: 10.1109/IGARSS.2009.5417532.

Pradhan, B., M. S. Tehrany, & M. N. Jebur. 2016. A New Semiautomated Detection Mapping of Flood Extent From TerraSAR-X Satellite Image Using Rule-Based Classification and Taguchi Optimization Techniques. IEEE Transactions on Geoscience and Remote Sensing **54**:4331-4342.

Qi, Z., A. G.-O. Yeh, X. Li, & Z. Lin. 2012. A novel algorithm for land use and land cover classification using RADARSAT-2 polarimetric SAR data. Remote Sensing of Environment **118**:21-39.

Qiang, Y. 2019. Disparities of population exposed to flood hazards in the United States. Journal of Environmental Management **232**:295-304.

Ramsey III, E., A. Rangoonwala, & T. Bannister. 2013. Coastal Flood Inundation Monitoring with Satellite C-band and L-band Synthetic Aperture Radar Data. JAWRA Journal of the American Water Resources Association **49**:1239-1260.

Ranger, C. M., M. E. Reding, P. B. Schultz, & J. B. Oliver. 2013. Influence of flood-stress on ambrosia beetle host-selection and implications for their management in a changing climate. Agricultural and Forest Entomology **15**:56-64.

Razavi, S., P. Gober, H. R. Maier, R. Brouwer, & H. Wheater. 2020. Anthropocene flooding: Challenges for science and society. Hydrological Processes **34**:1996-2000.

Rosen, P. A., S. Hensley, K. Wheeler, G. Sadowy, T. Miller, S. Shaffer, R. Muellerschoen, C. Jones, H. Zebker, & S. Madsen. 2006. UAVSAR: a new NASA airborne SAR system for science and technology research. Page 8 pp. *in* 2006 IEEE Conference on Radar.

Rubel, F., & M. Kottek. 2010. Observed and projected climate shifts 1901–2100 depicted by world maps of the Köppen-Geiger climate classification. Meteorologische Zeitschrift **19**:135-141.

Rueda, A., S. Vitousek, P. Camus, A. Tomás, A. Espejo, I. J. Losada, P. L. Barnard, L. H. Erikson, P. Ruggiero, B. G. Reguero, & F. J. Mendez. 2017. A global classification of coastal flood hazard climates associated with large-scale oceanographic forcing. Scientific Reports **7**:5038.

Sayemuzzaman, M., & M. K. Jha. 2014. Seasonal and annual precipitation time series trend analysis in North Carolina, United States. Atmospheric Research **137**:183-194.

Santoro, M., & U. Wegmüller. 2014. Multi-temporal Synthetic Aperture Radar Metrics Applied to Map Open Water Bodies. IEEE Journal of Selected Topics in Applied Earth Observations and Remote Sensing **7**:3225-3238.

Sanyal, J., & X. X. Lu. 2004. Application of Remote Sensing in Flood Management with Special Reference to Monsoon Asia: A Review. Natural Hazards **33**:283-301.

Schumann, G., G. Di Baldassarre, D. Alsdorf, & P. D. Bates. 2010. Near real-time flood wave approximation on large rivers from space: Application to the River Po, Italy. Water Resources Research **46**.

Schumann, G., R. Hostache, C. Puech, L. Hoffmann, P. Matgen, F. Pappenberger, & L. Pfister. 2007. High-Resolution 3-D Flood Information From Radar Imagery for Flood Hazard Management. IEEE Transactions on Geoscience and Remote Sensing **45**:1715-1725.

Schumann, G. J. P. 2014. Fight floods on a global scale. Nature **507**:169-169.

Schumann, G. J. P., & D. K. Moller. 2015. Microwave remote sensing of flood inundation. Physics and Chemistry of the Earth, Parts A/B/C **83-84**:84-95.

Shen, X., E. N. Anagnostou, G. H. Allen, G. Robert Brakenridge, & A. J. Kettner. 2019a. Near-real-time non-obstructed flood inundation mapping using synthetic aperture radar. Remote Sensing of Environment **221**:302-315.

Shen, X., D. Wang, K. Mao, E. Anagnostou, & Y. Hong. 2019b. Inundation Extent Mapping by Synthetic Aperture Radar: A Review. Remote Sensing **11**:879.

Shin, S., Y. Pokhrel, D. Yamazaki, X. Huang, N. Torbick, J. Qi, S. Pattanakiat, T. Ngo-Duc, & T. D. Nguyen. 2020. High Resolution Modeling of River-Floodplain-Reservoir Inundation Dynamics in the Mekong River Basin. Water Resources Research **56**:e2019WR026449.

Simard, M., B. V. Riel, M. Denbina, & S. Hensley. 2016. Radiometric Correction of Airborne Radar Images Over Forested Terrain With Topography. IEEE Transactions on Geoscience and Remote Sensing **54**:4488-4500.

Slater, L. J., & G. Villarini. 2016. Recent trends in U.S. flood risk. Geophysical Research Letters **43**:12,428-412,436.

Smith, L. C. 1997. Satellite remote sensing of river inundation area, stage, and discharge: a review. Hydrological Processes **11**:1427-1439.

Soille, P., & M. Pesaresi. 2002. Advances in mathematical morphology applied to geoscience and remote sensing. IEEE Transactions on Geoscience and Remote Sensing **40**:2042-2055.

Sokol, J., H. NcNairn, & T. Pultz. 2004. Case studies demonstrating the hydrological applications of C-band multipolarized and polarimetric SAR. Canadian Journal of Remote Sensing **30**:470-483.

Song, J. Y., P. Abbaszadeh, & H. Moradkhani. 2018. Future Probability of Hurricanes and their Uncertainties Across the South and East Coast of the US from Bayesian Perspective. Pages A11K-2389 AGU.

Thirion-Lefevre, L., & R. Guinvarc'h. 2018. The double Brewster angle effect. Comptes Rendus Physique **19**:43-53.

Townsend, P. A. 2002. Relationships between forest structure and the detection of flood inundation in forested wetlands using C-band SAR. International Journal of Remote Sensing **23**:443-460.

Twele, A., W. Cao, S. Plank, & S. Martinis. 2016. Sentinel-1-based flood mapping: a fully automated processing chain. International Journal of Remote Sensing **37**:2990-3004.

Ulaby, F. T., R. K. Moore, & A. K. Fung. 1986. Microwave remote sensing: Active and passive. Volume 3-From theory to applications.

UNISDR, C. 2015. The human cost of natural disasters: A global perspective.

Wang, C., Q. Gao, X. Wang, & M. Yu. 2015. Decadal trend in agricultural abandonment and woodland expansion in an Agro-Pastoral Transition Band in Northern China. Harvard Dataverse.

Wang, C., Q. Gao, X. Wang, & M. Yu. 2016. Spatially differentiated trends in urbanization, agricultural land abandonment and reclamation, and woodland recovery in Northern China. Sci Rep **6**:37658.

Wang, C., M. Yu, & Q. Gao. 2017. Continued Reforestation and Urban Expansion in the New Century of a Tropical Island in the Caribbean. Remote Sensing **9**:731.

Whelen, T., & P. Siqueira. 2017. Use of time-series L-band UAVSAR data for the classification of agricultural fields in the San Joaquin Valley. Remote Sensing of Environment **193**:216-224.

White, L., B. Brisco, M. Pregitzer, B. Tedford, & L. Boychuk. 2014. RADARSAT-2 beam mode selection for surface water and flooded vegetation mapping. Canadian Journal of Remote Sensing **40**:135-151.

Yang, L., S. Jin, P. Danielson, C. Homer, L. Gass, S. M. Bender, A. Case, C. Costello, J. Dewitz, J. Fry, M. Funk, B. Granneman, G. C. Liknes, M. Rigge, & G. Xian. 2018. A new generation of the United States National Land Cover Database: Requirements, research priorities, design, and implementation strategies. ISPRS Journal of Photogrammetry and Remote Sensing **146**:108-123.

Yao, F., C. Wang, D. Dong, J. Luo, Z. Shen, & K. Yang. 2015. High-Resolution Mapping of Urban Surface Water Using ZY-3 Multi-Spectral Imagery. Remote Sensing **7**:12336-12355.

Yao, F., J. Wang, C. Wang, & J.-F. Crétaux. 2019. Constructing long-term high-frequency time series of global lake and reservoir areas using Landsat imagery. Remote Sensing of Environment **232**:111210.

Zhang, M., Z. Li, B. Tian, J. Zhou, & P. Tang. 2016. The backscattering characteristics of wetland vegetation and water-level changes detection using

multi-mode SAR: A case study. International Journal of Applied Earth Observation and Geoinformation **45**:1-13.

Zhang, Z., W. Ni, G. Sun, W. Huang, K. J. Ranson, B. D. Cook, & Z. Guo. 2017. Biomass retrieval from L-band polarimetric UAVSAR backscatter and PRISM stereo imagery. Remote Sensing of Environment **194**:331-346.